

AD-A104 094

AUBURN UNIV ALA DEPT OF PHYSICS
INTENSE PULSED PROTON SOURCE (TIME AND WAVELENGTH RESOLVED STUDY--ETC(U))
JUN 81 J R WILLIAMS, J E GAISER

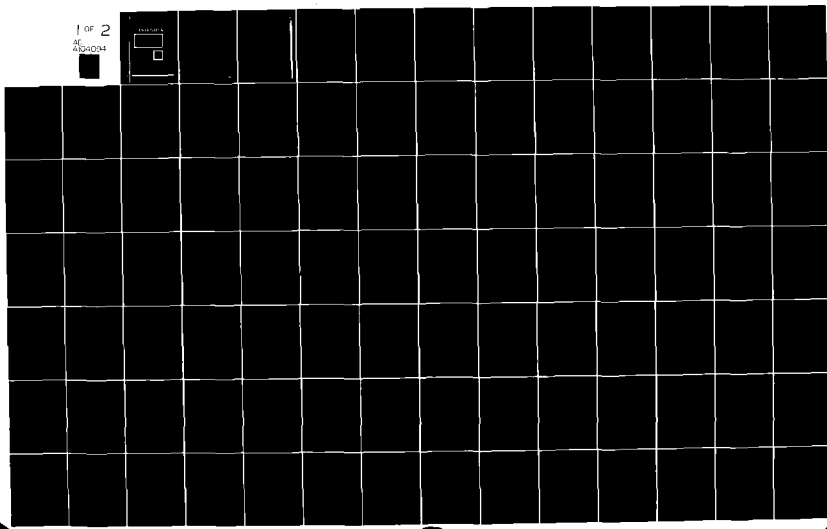
F/G 7/4

DASG60-79-C-0079

NL

UNCLASSIFIED

1 OF 2
AF ALQH034

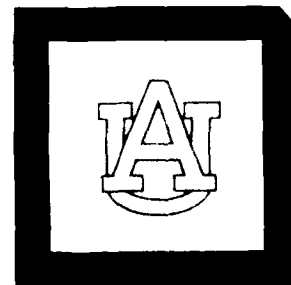


ADA104094

LEVEL III

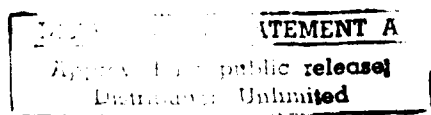
(2)

PHYSICS



AUBURN UNIVERSITY
AUBURN, ALABAMA

FILE COPY



OPTIC
ELECTRIC
SEP 11 1981

D

31723022

Accession No.	
File No.	X
Date:	
Unclassified	
Justification	
By Per Ltr. on file	
Distribution/	
Availability Copies	
Dist	Avail as is or Special
A	

INTENSE PULSED PROTON SOURCE (TIME AND WAVE-
LENGTH RESOLVED STUDIES OF XENON, LIQUID
XENON, AND XeF₂)

DASG60-79-C-0079

Final Contractor's Report

January 29, 1981

(Revision - June 26, 1981)

by

John R. Williams

James E. Gaiser

<input type="checkbox"/>	STATEMENT A
<input type="checkbox"/>	public release
<input type="checkbox"/>	Classification Unlimited

The views, opinions, and/or findings contained in this report are those of the authors and should not be construed as an official Department of the Army position, policy, or decision, unless so designated by other official documentation.

Physics Department

Auburn University, AL

36849

DTIC
SELECTED
SEP 11 1981
S D
D

REPORT DOCUMENTATION PAGE		READ INSTRUCTIONS BEFORE COMPLETING FORM
1. REPORT NUMBER	2. GOVT ACCESSION NO.	3. RECIPIENT'S CATALOG NUMBER
4. TITLE (and Subtitle) Intense Pulsed Proton Source (Time and Wavelength Resolved Studies of Xenon, Liquid Xenon, and XeF ₂)		5. TYPE OF REPORT & PERIOD COVERED Final Contractors Report May 31, 1979 - Jan 29, 1981
7. AUTHOR(s) John R. Williams James E. Gaiser	6. CONTRACT OR GRANT NUMBER(s) DASG60-79-C-0079	
9. PERFORMING ORGANIZATION NAME AND ADDRESS Physics Department Auburn University, AL 36849	10. PROGRAM ELEMENT, PROJECT, TASK AREA & WORK UNIT NUMBERS 6 u 11	
11. CONTROLLING OFFICE NAME AND ADDRESS Ballistic Missile Defense Advanced Technology Center, P.O. Box 1500, Huntsville, AL 35807	12. REPORT DATE January 29, 1981	
14. MONITORING AGENCY NAME & ADDRESS (if different from Controlling Office)	13. NUMBER OF PAGES 95	
	15. SECURITY CLASS. (of this report) Unclassified	
	15a. DECLASSIFICATION/DOWNGRADING SCHEDULE	
16. DISTRIBUTION STATEMENT (of this Report) DISTRIBUTION STATEMENT Approved for public release Distribution Unlimited		
17. DISTRIBUTION STATEMENT (of the abstract entered in Block 20, if different from Report)		
18. SUPPLEMENTARY NOTES		
19. KEY WORDS (Continue on reverse side if necessary and identify by block number) Xe*, Xe ₂ , liquid xenon, absolute efficiency, photodissociation, XeF ₂ , destruction frequency, rate constant, excited state lifetime		
20. ABSTRACT (Continue on reverse side if necessary and identify by block number) Time and wavelength resolved spectroscopic measurements have been performed for xenon gas excited by 2.0 MeV protons. Reaction rate constants for the formation and decay of the ³ Σ_u^+ and the ¹ Σ_u^+ states in Xe ₂ * via three body collisions are 31 Hz/Torr ² and 61 Hz/torr ² , respectively. A kinetic model based on the experimental facts is presented and is examined. The lifetime of the ³ Σ_u^+ state in Xe ₂ * has been measured to be 102 ns. Single proton counting		

techniques were used, and both the 172 nm radiation from the $^3\Sigma_u$ state as well as the 152 nm radiation from the $^1\Sigma_u$ state were monitored as a function of time and pressure. The rate constants of interest have been extracted from the pressure dependence of the decay times. Ion recombination kinetic processes were clearly distinguishable at higher pressures and could be dealt with independently from the excited state channel reactions. Tests were performed to insure that events which occur late in time following excitation were actually ion recombination processes. Absolute conversion efficiencies were measured for proton energy input to 172 nm proton energy output. Photodissociation of XeF_2 to form XeF(B) and XeF(C) via the reactions



was attempted using 172 nm photons from Xe_2^* . Population of the XeF(B) state was observed, and the B state fluorescence at 351 nm decreased with increasing Ar buffer gas pressure. However no corresponding increase was observed for the XeF(C) state at 483 nm.

TABLE OF CONTENTS

LIST OF TABLES.....	viii
LIST OF FIGURES.....	ix
I. INTRODUCTION.....	1
II. EXPERIMENTAL PROCEDURE.....	10
III. EXPERIMENTAL RESULTS.....	34
IV. KINETIC MODEL.....	51
V. DISCUSSION AND SUMMARY.....	59
LIST OF REFERENCES.....	64
APPENDIX A.....	66
APPENDIX B.....	72
APPENDIX C.....	82
APPENDIX D.....	89
APPENDIX E.....	92

LIST OF TABLES

1. Summary of previously measured rate constants.....	6
2. Physical composition of HAVAR	68
3. Radiant emittance from D ₂ lamp by NBS.....	75
4. Fitting parameters for absolute efficiency.....	80

LIST OF FIGURES

1. Potential Curves for Xe_2^*	2
2. Accelerator and Beam Transport System.....	11
3. Scintillation Cell and Monochromators.....	13
4. Gas Handling System.....	14
5. Electronics in SPC System.....	16
6. SPC Region of PMT.....	18
7. Time Resolved Data-147 nm.....	22
8. Time Resolved Data-172 nm.....	22
9. Time Resolved Data-152 nm.....	23
10. Time Resolved Data-Expanded Time Scale $P_{\text{N}_2} = 0$	24
11. Time Resolved Data-Expanded Time Scale $P_{\text{N}_2} = 0.09$	25
12. Xenon Scan-2500 Torr.....	27
13. Liquid Xenon Cell.....	29
14. Liquid Xenon Scan.....	30
15. XeF_2 Photodissociation Cell.....	32
16. XeF_2 Scan.....	33
17. XeF (B-X) Decay.....	34
18. Destruct. Freq. vs. Pressure-147 nm.....	37
19. Destruct. Freq. vs. Pressure-152 nm.....	38
20. Destruct. Freq. vs. Pressure-172 nm- $P < 200$ Torr.....	40
21. Destruct. Freq. vs. Pressure-172 nm- $P > 200$ Torr.....	41
22. Intensity vs. Wavelength vs. Pressure.....	43
23. Pressure Dependence of VUV Intensity.....	44

24.	Absorption of D ₂ Lamp by XeF ₂ Cell.....	46
25.	B and C State Emissions-All Buffer Gas Press.....	47
26.	Conversion Efficiency vs. Pressure.....	52
27.	Summary of Kinetic Processes.....	54
28.	Setup for Monochromator Calibration.....	76
29.	Monochromator Efficiency vs. Wavelength.....	81

I. INTRODUCTION

The rare gas excimer systems, as candidates for high power and high efficiency lasers in the vacuum ultraviolet (VUV), have been of considerable interest in the past decade. The expected high efficiency of these lasers has yet to be achieved¹. A complete understanding of the kinetic processes in the excimer systems is therefore necessary to comprehend fully the energy pathways taken during excitation and deexcitation. Fluorescence spectroscopy is one means of studying these processes and has been most useful in the determination of reaction rate constants and radiative lifetimes.

Figure 1 shows the energy levels of the low lying states in Xe and Xe_2^* . The repulsive ground state and bound excited states are characteristic of all the rare gas excimers. The lower atomic state (${}^3\text{P}_2$) is metastable and is generally believed to be the precursor of the ${}^3\Sigma_u^-$ molecular state through three body interactions. The upper atomic state (${}^3\text{P}_1$) is the resonance state and is thought to be the precursor of the ${}^1\Sigma_u^+$ state in Xe_2^* . Atomic state mixing results from two body collisions with ground state atoms. All the above mentioned processes must be considered in the development of the reaction kinetics.

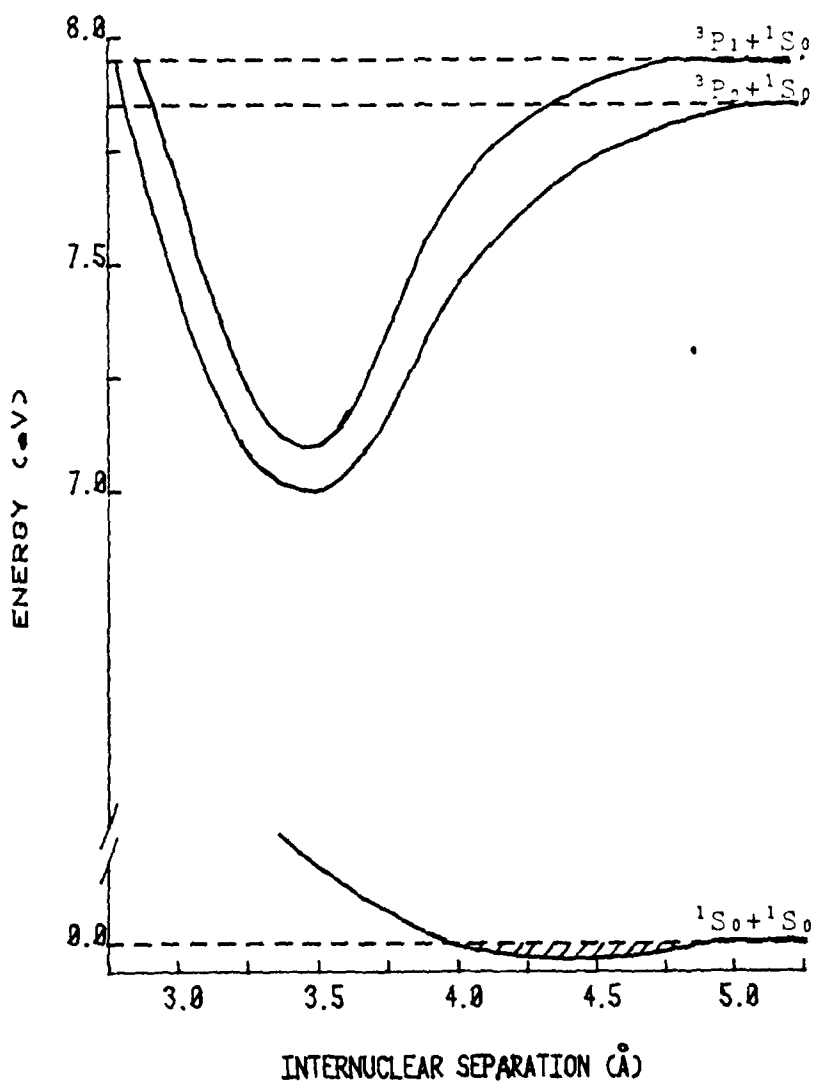


Figure 1. Potential curves for Xe_2^* . Shaded region is the van der Waals ground state in Xe_2 . The dashed lines correspond to infinite separation of the two atoms in the states shown on the right.

Early work by Colli² was performed using a Townsend discharge with argon as the rare gas. Although the time resolution of 0.5 μ s for his experiment is considered poor by modern day standards, he was able to predict the formation and subsequent decay of the Ar₂^{*} molecule and determine reaction rate constants.

In the past decade considerable work has been done using xenon. Keto^{3,4} used a low intensity electron beam for excitation and determined the reaction rate constants together with the radiative lifetimes of the excimer states. These rate constants and lifetimes were obtained by time resolved spectroscopy following excitation. By using very high pressures (>30 atmospheres) Keto could determine the radiative lifetime of both the low-lying states in Xe₂^{*}. On the other hand, Timpson and Anderson⁵ used optical pumping techniques at extremely low pressures (<15 Torr) and found that two and three body collisions were necessary to account for the pressure dependence of the VUV radiation detected.

Johnson and Geraldo⁶ used a high pressure gas cell in conjunction with a high current (>15 kA) electron accelerator. This study was performed under pseudo-laser conditions in the attempt to study ion channel kinetics in the deexcitation of Xe₂^{*}. Bouciouq and Mortier⁷ used a Townsend discharge while Millet⁸ used alpha particles

for excitation and single photon counting techniques to detect the VUV fluorescence. Leichner⁹ used a low intensity electron beam and a pressure range of 100 to 1000 Torr to determine the rate constants and radiative lifetimes for the formation and decay of the $^3\Sigma_u$ and the $^1\Sigma_u^*$ states in Xe_2 . Theoretical calculations and discussions have been presented by Mullikan¹⁰ and Ermler¹¹. Ermler gives estimates of the radiative lifetimes for the molecular states.

The necessity for selective excitation to either the resonance or metastable atomic states was soon recognized as a method to distinguish between the two excimer states which are formed from collisions of the excited atoms with ground state atoms. The recent availability of synchrotron radiation as a tunable source of VUV photons has led to experiments which allow the selective excitation of the atomic and molecular states. Gelfenstien¹² and Dutuit¹³ have performed these experiments at the Orsay Electron Storage Ring; however their results are in serious disagreement, even when they used the same equipment. Thornton¹⁴ has used the Stanford Synchrotron Radiation Laboratory as a source of VUV photons for direct excitation of the upper vibrational levels of the excimer states from the van der Waals ground state. Direct excitation of the lower vibrational levels was not

possible due to the small Frank-Condon overlap of the upper states with the bound region of the ground state molecule.¹⁴ A summary of the previously reported rate constants and radiative lifetimes is given in Table 1.

As noted in Table 1, serious discrepancies exist between the results of different authors. The high power experiments give rise to other reactions (e.g. ion channel effects) which can mask the effects of the excited state channels. The older works cannot be expected to agree with more recent experiments due to the improvements in experimental equipment during the past decade.

The present experiments were undertaken with the goal of determining the energy pathways followed in the formation and decay of the Xe_2^* molecule. Pulsed protons from a 3 MV accelerator were used for excitation. The low energy deposition per proton pulse and variable repetition rate allowed for complete control of experimental parameters.

Using published tables of energy loss per unit path length^{15,16}, the energy deposited in the interaction region can be calculated. Using beam intensities of approximately 10^7 protons per pulse and with the assumption that 25 eV are required to form an ion-electron pair, one can show that there are still $\approx 10^7$ more neutral atoms present in the interaction region than there are ions.

Table 1. Previously measured rate constants and lifetimes
for Xe and Xe₂. † denotes theoretical calculation.

Reaction	Rate Constant	Lifetime	Ref.
Xe(³ P ₂) + 2Xe(¹ S ₀) → Xe ₂ [*] (³ Σ _u) + Xe	80 Hz/Torr ²	5	
	24 Hz/Torr ²	7	
	78 Hz/Torr ²	8	
	36 Hz/Torr ²	9	
	87 Hz/Torr ²	16	
Xe(³ P ₁) + 2Xe(¹ S ₀) → Xe ₂ (¹ Σ _u) + Xe	46 Hz/Torr ²	9	
Xe(³ P ₂) + Xe(¹ S ₀) → 2Xe(¹ S ₀) + hν	71 Hz/Torr	9	6
Xe(³ P ₂) + Xe(¹ S ₀) → Xe(³ P ₁) + Xe	49 Hz/Torr	9	
Xe(³ P ₁) + Xe(¹ S ₀) → Xe(³ P ₂) + Xe	9100 Hz/Torr	9	
Xe(³ Σ _u) → 2Xe(¹ S ₀) + hν	96 ns	3	
	500 ns	7	
	102 ns	8	
	99 ns	9	
	172+ ns	11	
	112 ns	14	
Xe(¹ Σ _u) → 2Xe(¹ S ₀) + hν	6.2 ns	3	
	5.5† ns	11	
	2.1 ns	14	

The ion recombination reaction rate is proportional to the product of the ion population and the electron population, while the excited state reaction rate is proportional to the product of the excited state population and the square of the neutral population. Symbolically this is written as

$$R_{ion} \sim k_{ion} (Xe^+) (e^-) \quad 1)$$

$$R_{ex} \sim k_{ex} (Xe^*) (Xe)^2. \quad 2)$$

For the beam induced plasma, the ion population, electron population, and the excited state population are all of the same order of magnitude, while the neutral atom population is many orders of magnitude greater, as discussed in the previous paragraph. We see from Eqs. 1 and 2 that the excited state reaction rate will be considerably faster than the ion recombination rate even if the ion recombination rate constant, k_{ion} , is larger than the excited state rate constant, k_{ex} , by two or three orders of magnitude.

Detailed calculations have been done by Dr. Edward Fisher at Wayne State University which show that the ion population and the excited state population produced by a 2 MeV proton beam are essentially equal¹⁷. The electron population must reflect the ion population as they are produced in a one-to-one relationship to each other.

Hence it is assumed that all ion channel kinetics can be safely neglected. For this same reason, that is, that there are few ions in the system compared to the number of atoms present, there are also few free electrons in the system. It is therefore assumed that all electron mixing of atomic and molecular states can be neglected.

Collisionally induced mixing of the molecular states was neglected due to the low pressures used*, however mixing of the atomic states ($^3P_1 \pm ^3P_2$) due to collisions was included in the development of the kinetics. The pressure range of 5 to 1200 Torr for the time resolved and 100 to 2500 Torr for the wavelength resolved spectroscopy was chosen such that both the first and second continua near 150 and 170 nm, respectively could be observed. The extreme low pressures were used for the observation of the 3P_1 resonance radiation at 147 nm. Single photon counting techniques were used in conjunction with conventional nuclear electronics.

Absolute intensity measurements of the first and second continua were performed in an attempt to determine the conversion efficiency from proton energy deposited in the gas to photon energy emitted in the decay of the molecular species.

Photodissociation of the XeF_2 molecule using radiation from the second continuum of Xe_2^* was attempted in the presence of a buffer gas in an effort to enhance the C state in XeF^* emission at 480 nm with respect to the B state in XeF^* emission at 351 nm. Ar was used as a buffer gas and the Ar pressure was varied from 0 to 2325 Torr.

Experimental details are discussed in Chapter II, and experimental results are presented in Chapter III. A kinetic scheme for the Xe-Xe_2^* system, based on experimental findings, is presented in Chapter IV, and the results are discussed in Chapter V.

II. EXPERIMENTAL PROCEDURE

Accelerator and Beam Transport System

All experiments were performed at the Nuclear Science Center using the 3 MV Dynamitron accelerator. Pulsed protons were produced in a Duoplasmatron ion source, accelerated to the desired energy in the accelerator, momentum analyzed in an NMR controlled electromagnet and focused on target. Further discussion of the accelerator and beam transport system can be found in reference 18.

Figure 2 shows a schematic overview of the accelerator and experimental area used in conjunction with this work. Beam pulse width measurements were carried out using a fast Faraday cup mounted in the scattering chamber. The Faraday cup was designed by Harper¹⁹. A pulsed proton beam was incident on the Faraday cup which was connected to a Tektronix 3S2 sampling oscilloscope by approximately one meter of RG-8U coaxial cable. With this method the pulse width was measured to be 1.1 nsec FWHM. Transmission measurements were also carried out with a 5.14×10^{-4} cm Havar foil which served as the

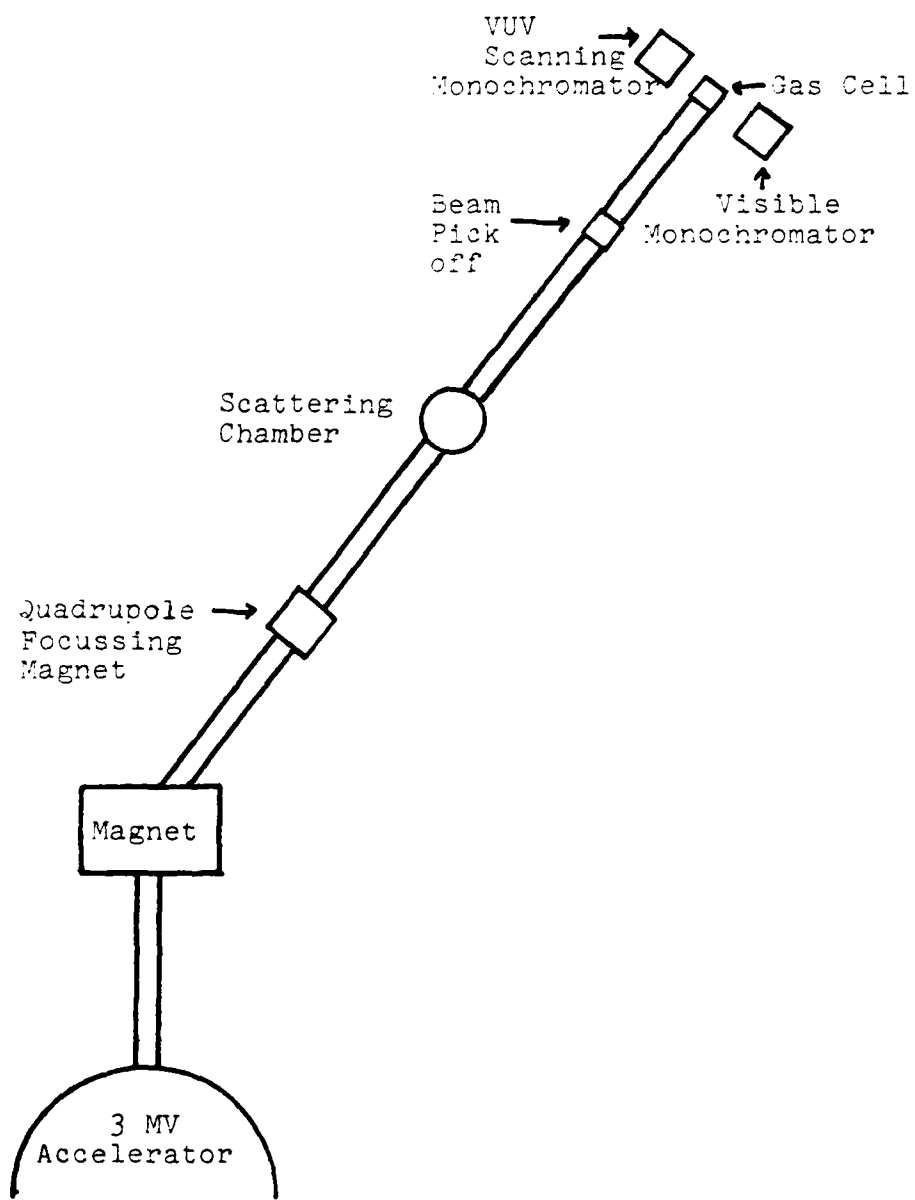


Figure 2. Accelerator and Beam Transport System

entrance foil for the scintillation cell. The transmission of the foil was measured and found to be essentially 100%. Energy loss calculations were performed for the foil and are discussed in Appendix A.

A beam pick off (BPO) was positioned axially in the beam line and was used to signal the arrival of the beam pulse from the accelerator. The signal produced by the BPO was used as a time reference in the electronics system during data acquisition.

Scintillation Cell and Gas Handling System

The scintillation cell for all gaseous experiments was a stainless steel cylinder provided with two viewing ports for diagnostics. The scintillation cell is shown in Figure 3. The 3.8 cm diameter CaF_2 windows provided about 90% transmission in the VUV. A detachable side chamber was provided for photodissociation measurements with XeF_2 .

The gas handling system consisted of high purity xenon gas, regulator, mass flow meter, and pressure sensor. This system is diagramed in Figure 4. The xenon gas was obtained from Matheson and Air Products and had a stated purity of 99.95%. The largest impurity was krypton at <35 ppm. All gas lines were standard 0.25 inch copper tubing equipped with Swagelock fittings. The mass flow

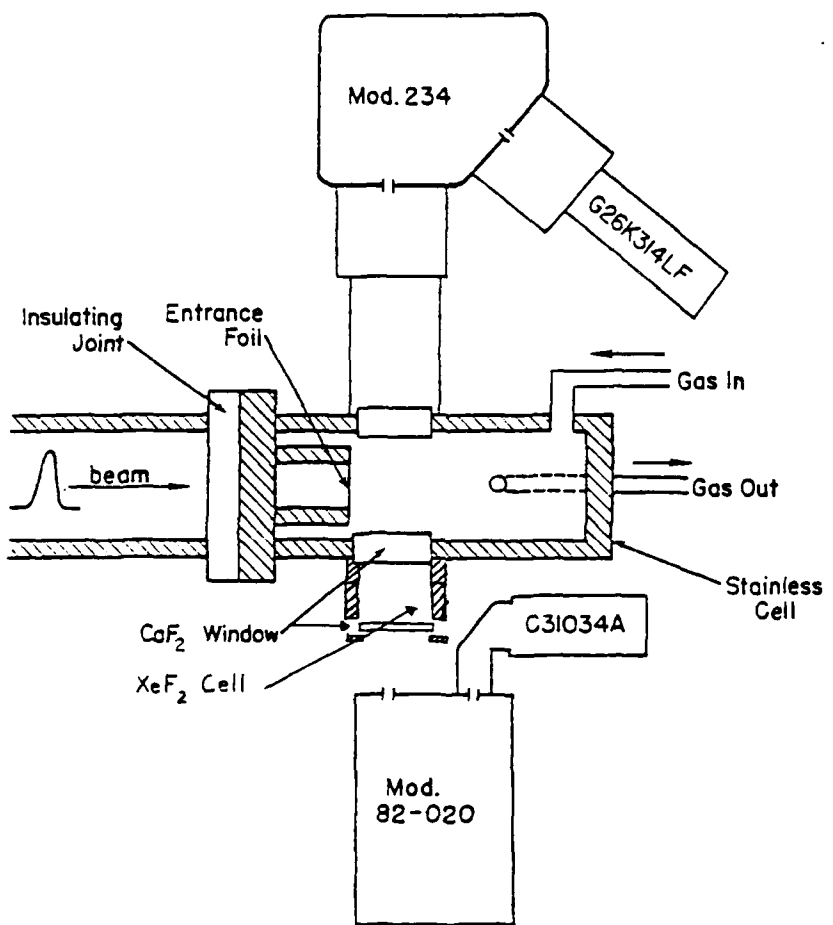


Figure 3. Scintillation Cell and Monochromators

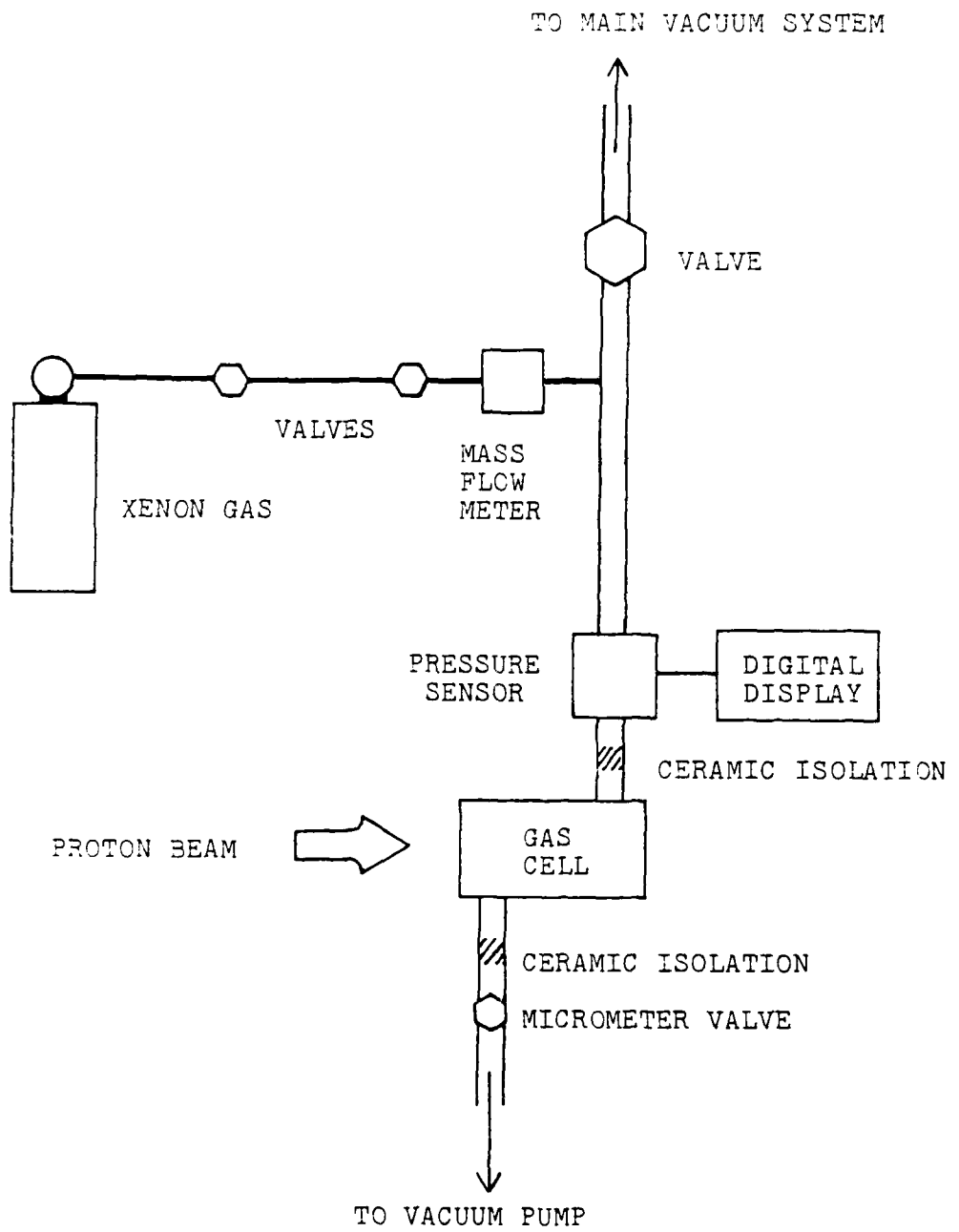


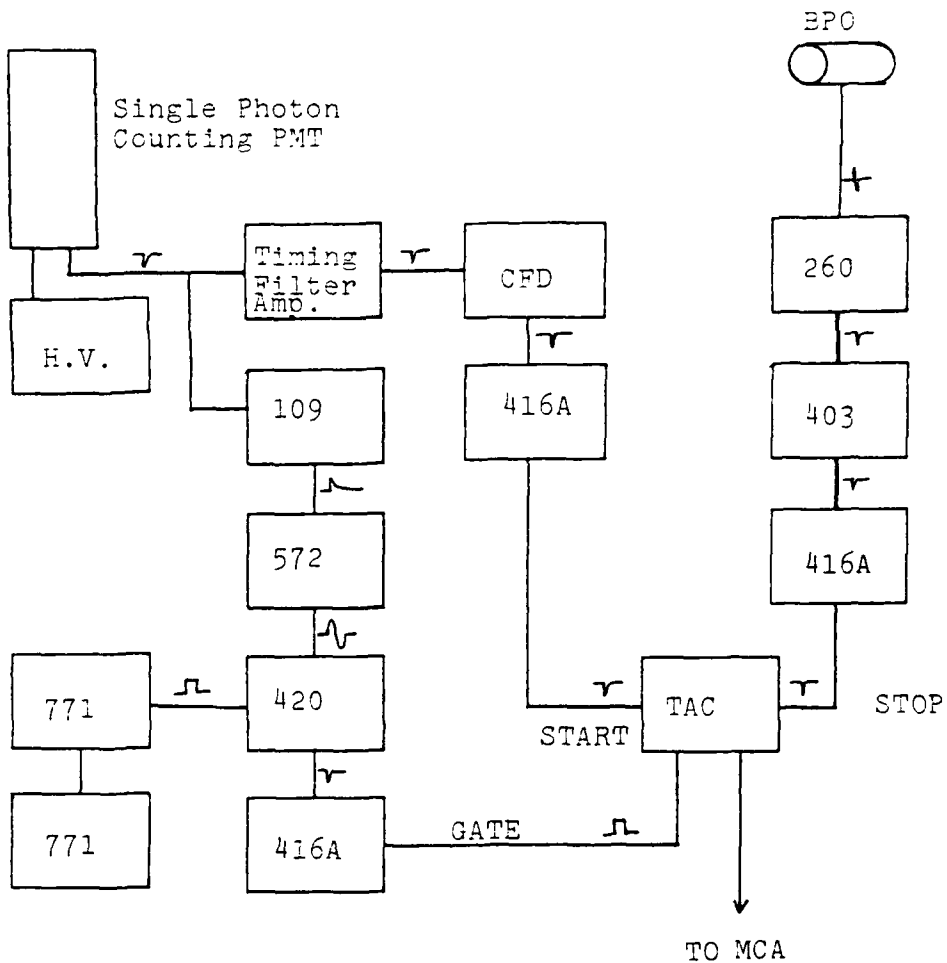
Figure 4. Gas Handling System

meter was manufactured by Hastings and had a range of 0 to 50 standard cubic centimeters per minute (SCCM). Calibration of the flow meter was accomplished using a flow meter calibrator which was traceable to NBS. This system allowed steady flow conditions to be reproduced.

Single Photon Counting System

A single photon counting (SPC) system was used in conjunction with a McPherson 234 monochromator. The monochromator was equipped with a 5.08 cm oil diffusion pump and a Freon cooled cold trap which provided oil free operation down to 3.6×10^{-6} Torr. The grating used has 1200 grooves per mm and a wavelength range from 100 to 300 nm. A SPC photomultiplier manufactured by EMI was used as the VUV photon detector. A complete description of the SPC system has been previously reported and only a general outline will be given here¹⁸.

A block diagram of the electronics in the SPC system is shown in Figure 5. The BPO is shown for completeness and provides a time reference as previously described. Photons which strike the photocathode provide two usable signals after preamplification. A timing signal is produced by the constant fraction discriminator (CFD) and a linear signal is produced by the main amplifier. The linear signal is used to determine the single photon



ORTEC NUMBERS

- 109-Preamp
- 260-Time Pick Off
- 416-Gate and Delay
- 771-Timer/Counter
- 572-Amplifier
- 403-Time Pick Off Control
- 420-Timing Single Channel Analyzer

Figure 5. Electronics in Single Photon Counting System.

counting range of the PMT while the CFD output is used strictly as a timing signal and is used as a 'START' signal for the time to amplitude converter (TAC). The pulse height spectrum of the signal from the main amplifier is shown in Figure 6. The low amplitude signals result from the dark noise of the tube, the center segment corresponds to the single photon counting region while the large amplitude signals originate from multiple photon events. A single channel analyzer (SCA) followed the main amplifier and was used to select the single photon counting region. This region is also shown in Figure 6. The slow logic output of the SCA provided a signal for each single photon event that occurred and was used as a gate for the TAC whenever lifetimes of excited states were measured. The gate was necessary since the 'START' signal (provided by the CFD) was present from multiple as well as single photon events. This is because the CFD acts as an integral discriminator whereas the SCA acts as a differential discriminator.

The system was also capable of operating in the scan mode. In this mode the slow logic output of the SCA was multiscaled as the wavelength band of the monochromator was stepped. In this manner an intensity spectrum of the system under investigation could be obtained.

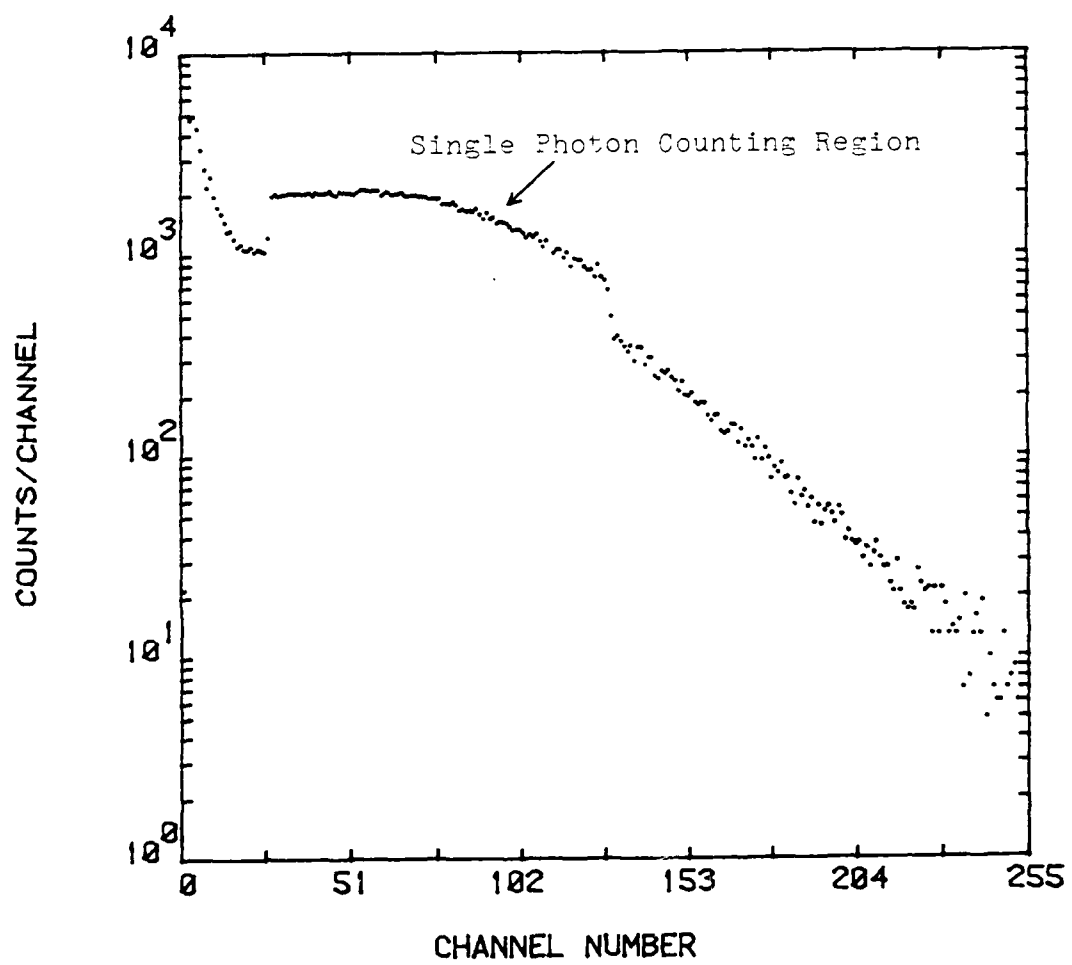


Figure 6. Pulse Height Analysis of PMT Anode Signal.

Data Acquisition

Data for all experiments was acquired using multi-channel analyzers (MCA). When excited state lifetimes and decay rates were determined, the MCA was used in the pulse height analysis mode and the TAC output was digitized and recorded. In the scan mode the SCA slow logic pulses were multiscaled and other parameters of interest were recorded. These included the pressure used in the all gas experiments as well as in the liquid experiment where the temperature was also monitored and recorded. When a scan was taken, the beam current integrator output was also multiscaled simultaneously with a second MCA. This allowed for correction of the intensity due to small changes in the beam current during the course of a run.

All the multichannel analyzers used in the present experiments were interfaced to a nine track magnetic tape drive for data storage. For offline analysis, an IBM 3031 computer was used as well as a Tektronix 4051 minicomputer.

Time Resolved Experiments

In the time resolved work, one of the principal objectives was to determine the excited state channel reaction rates as a function of pressure and determine the reaction rate constants of interest. By using the

techniques described in the previous section, the reaction rates were measured for the 172 nm Xe_2^* band (second continuum), the 147 nm resonance line, and the 152 nm Xe_2^* band (first continuum). It was necessary to set the Xe flow rate at a minimum of 50 SCCM in order to achieve reproducibility.

For the 147 nm resonance line the pressure ranged from 5 Torr to 75 Torr. Above 80 Torr the line disappeared completely and no data could be taken. A typical time resolved spectrum at 147 nm is given in Figure 7. The solid line is the least squares fit to the data using a two component exponential curve fitting routine²⁰ based on the Marquardt algorithm²¹.

Data for the 172 nm band from Xe_2^* was taken at a wide variety of pressures ranging from 50 Torr where it was first observed through 1200 Torr. A time resolved spectrum at 172 nm is shown in Figure 8. Again the solid line is a least squares two component exponential fit to the data.

The first continuum at 152 nm was also observed using time resolved techniques. Its decay is very similar to that of the second continuum and Figure 9 is representative time resolved spectrum. The dip seen in Figure 9 results from the ion recombination process

discussed in the introduction. This dip is shown on an expanded time scale in Figure 10. The dip was first observed at a pressure of 600 Torr and was seen in the decay of both the 172 nm second continuum and the first continuum at 152 nm. The dip was never seen in data taken at the 147 nm resonance line. As seen in Figure 10, there are two relative maxima separated by a time of about 650 ns. This time difference was essentially a constant over the pressure range from 600 Torr to 1200 Torr.

To show conclusively that the dip and second rise are due to ion channel processes, a small amount of nitrogen (<.1 Torr) was added to the xenon. The xenon pressure was 1000 Torr. The time resolved spectrum obtained under these conditions is shown in Figure 11. As we see in Figure 11, the dip and second maximum are no longer present. This is due to the nitrogen soaking up all the free electrons in the system, so that no electrons are available to participate in the ion processes. With this information at hand, it was then possible to analyze data taken at high pressures only on short time scales compared to the ion recombination times, hence neglecting these effects.

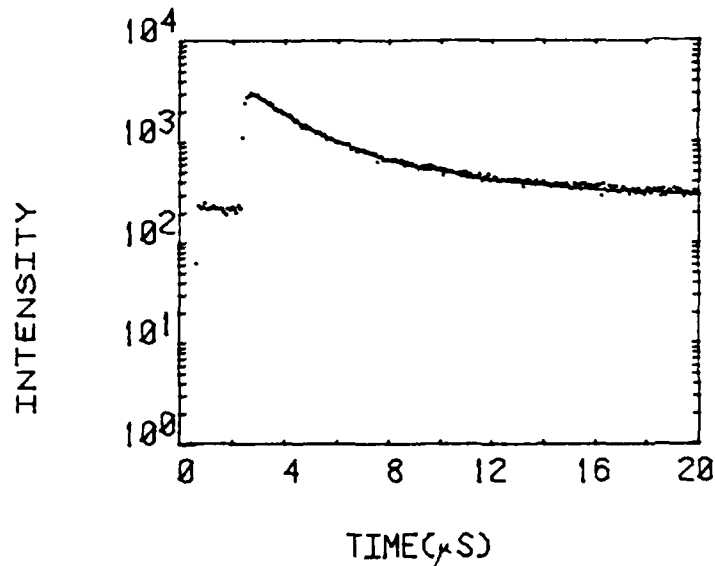


Figure 7. Typical time resolved data at 147 nm.

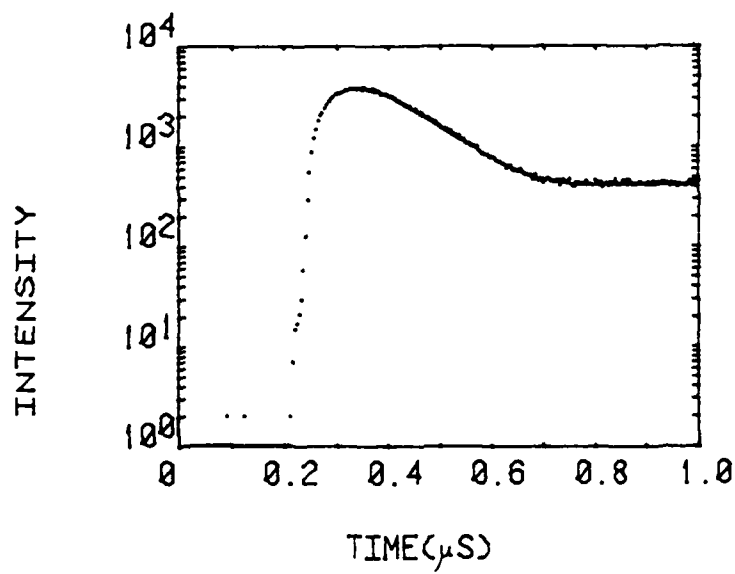


Figure 8. Typical time resolved data at 172 nm.

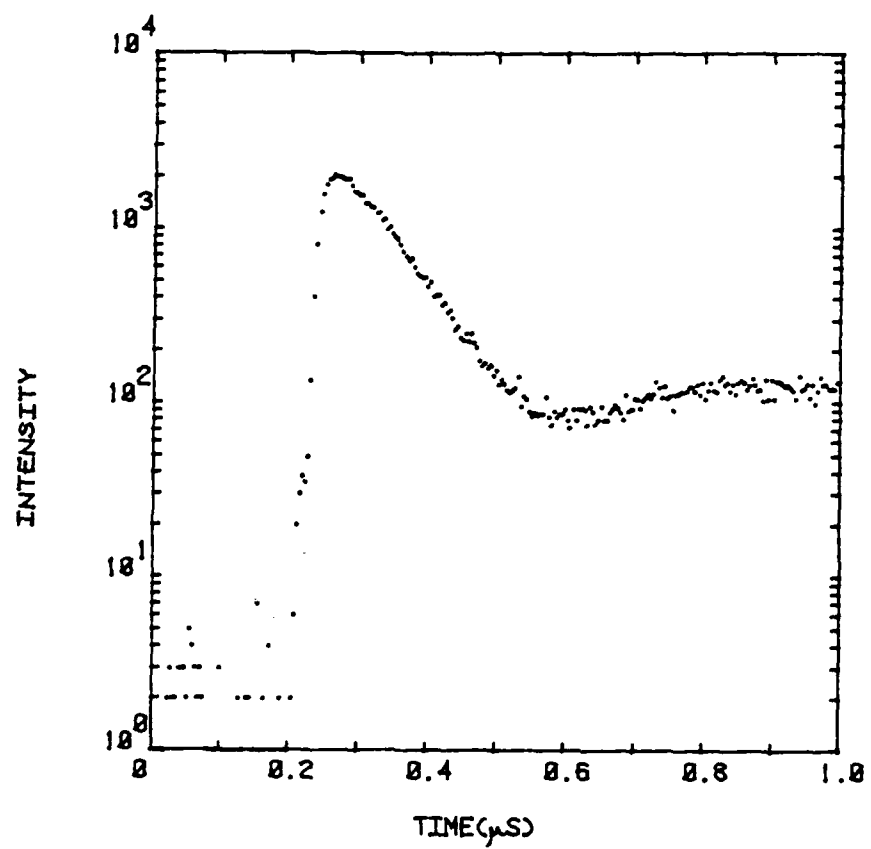


Figure 9. Typical Time Resolved Data-152 nm.
Xenon Pressure is 800 Torr.

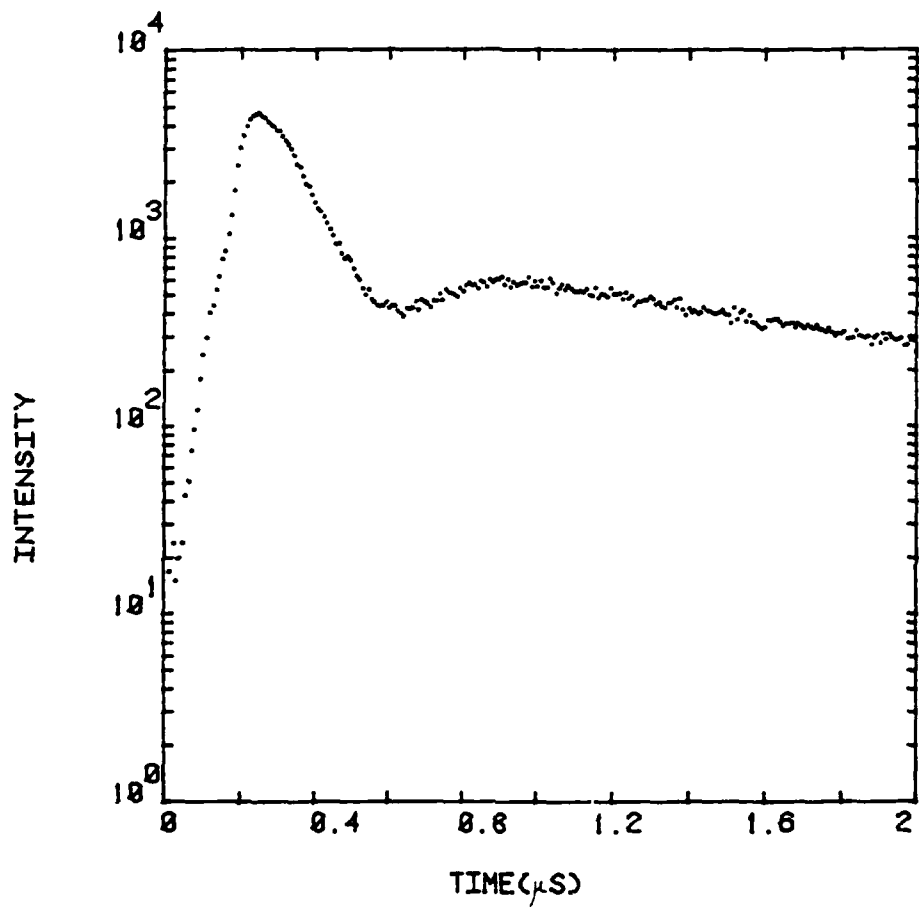


Figure 10. Time resolved spectrum at 172 nm.
Time scale expanded to show dip.
 $P_{Xe} = 1000 \text{ Torr}$, $P_{N_2} = 0$.

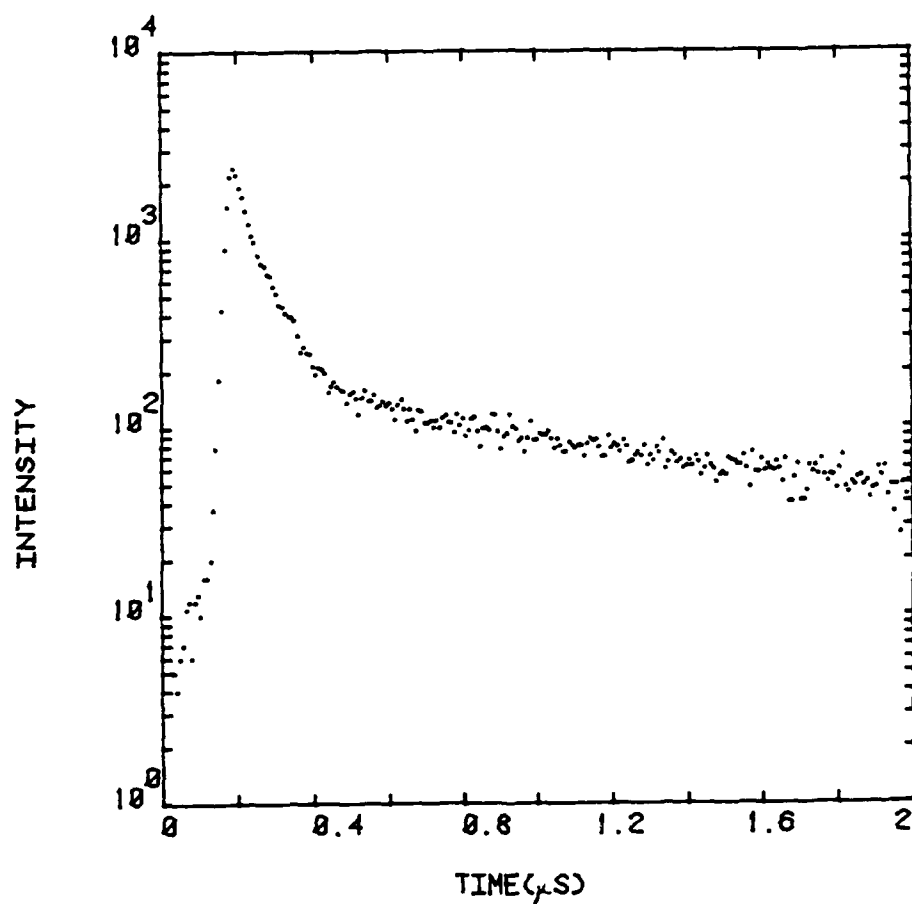


Figure 11. Time resolved spectrum at 172 nm.
 $P_{Xe} = 1000$ Torr, $P_{N_2} = .09$ Torr.

Wavelength Resolved Experiments

All wavelength resolved spectra were acquired using the monochromator in the scanning mode. Emission spectra were obtained from 500 to 2500 Torr in 500 Torr steps. As mentioned previously the integrated beam current was multiscaled simultaneously with the PMT output for normalization purposes. All scans were taken at a scan speed of 2 nm/min with entrance and exit slit settings of 130 μm . A typical scan is shown in Figure 12. The pressure dependence of the total intensity in the 172 nm band was determined and will be discussed in Chapter IV.

The monochromator was calibrated absolutely using a D₂ gas discharge lamp manufactured by Hamamatsu Co. The lamp was calibrated by the Radiometric Physics Division of the National Bureau of Standards. NBS provided a list of wavelengths and corresponding power densities. The power density (W/cm^3) was converted to photon flux per nanometer ($\text{photons}\cdot\text{cm}^{-2}\cdot\text{sec}^{-1}\cdot\text{nm}^{-1}$) by the formula

$$\phi = 5.03 \times 10^8 \cdot \lambda \cdot P$$

where λ is expressed in nm and P is the power density corresponding to λ , specified by NBS. By using the prescription given by NBS for the operation of the lamp²², the absolute efficiency of the monochromator and associated optical system could be determined. Appendix B contains the entire calibration procedure used on this experiment.

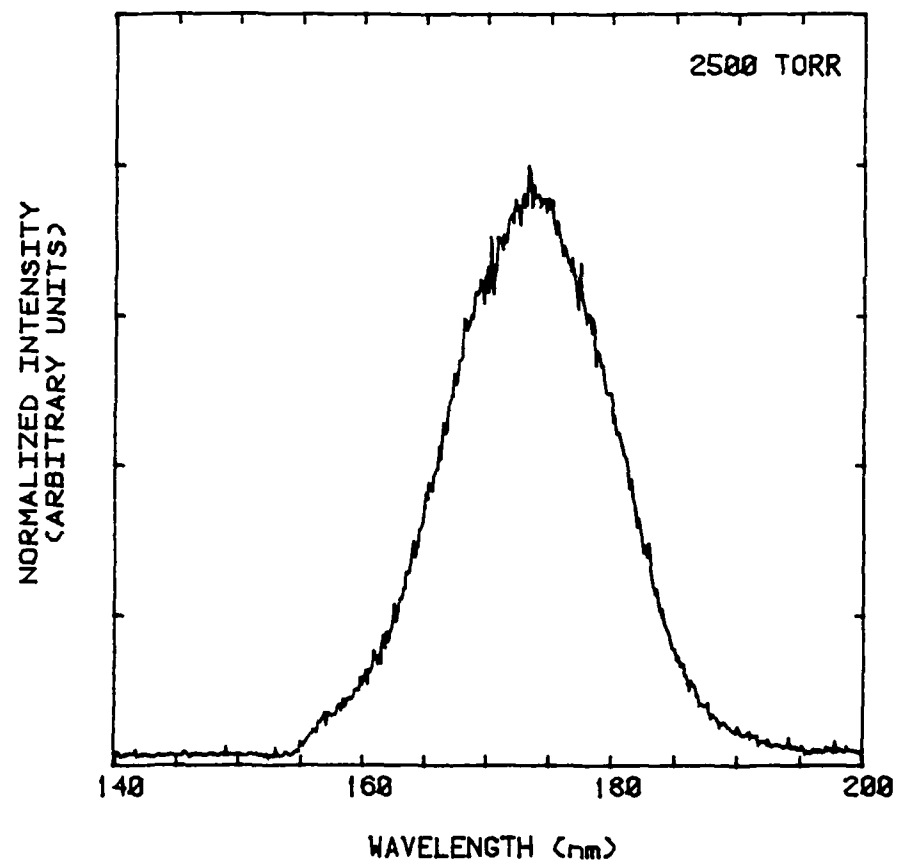


Figure 12. Wavelength Scan of 2500 Torr Xenon.

Liquid Xenon Experiments

Emission spectra were also obtained for liquid xenon excited by pulsed protons. The scintillation chamber is shown in Figure 13 and was made of brass with an inner diameter of 0.635 cm. LN₂ cooling lines were provided and the cell temperature was maintained at 193°K as measured by a platinum resistance thermometer. The temperature was maintained by controlling the flow of LN₂ blowoff from a dewar pressurized to 15 psig.

The cell was mounted on ceramic standoffs, for electrical and thermal isolation, to a 15.24 cm brass plate and enclosed by a stainless steel vacuum chamber equipped with standard UHV fittings. A CaF₂ window was attached to the rear of the cell using a 2.54x10⁻³ cm thick lead washer as a seal. A mirror and plexiglass window at 90° allowed the liquid level to be monitored periodically during the course of the run. The liquid xenon scan is shown in Figure 14. Note that the scan is simply a normalized scan and not in absolute units.

XeF₂ Photodissociation Experiments

Experiments were also conducted for the photodissociation of XeF₂ by 172 nm photons from Xe₂^{*}. XeF₂, which is a stable, white powder at room temperature and atmospheric pressure, was placed in the small, side chamber

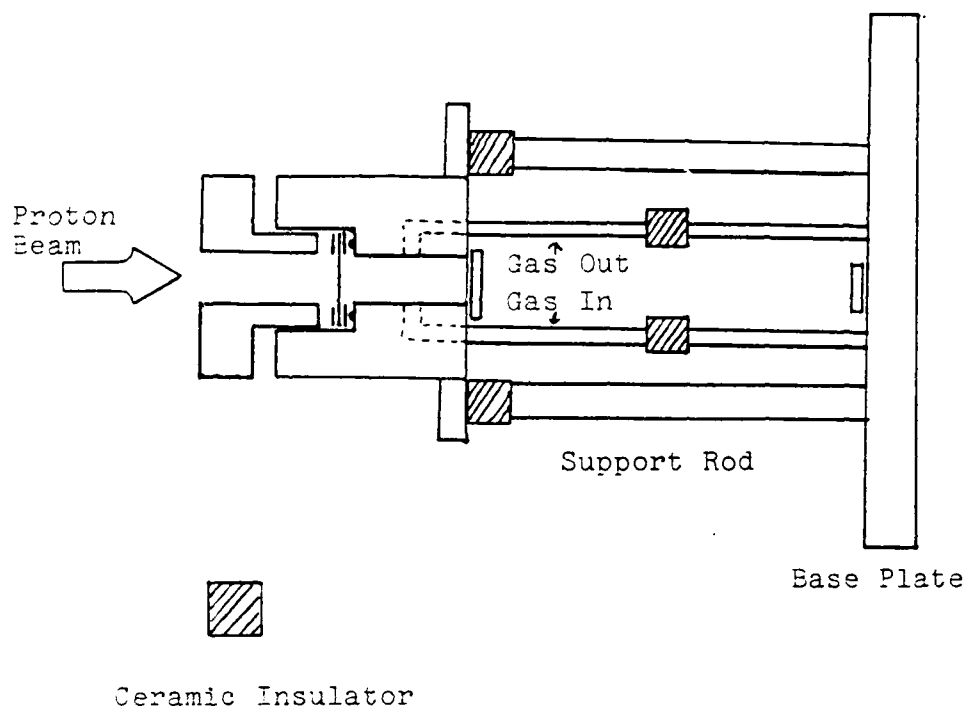


Figure 13. Liquid Xenon Scintillation Cell.

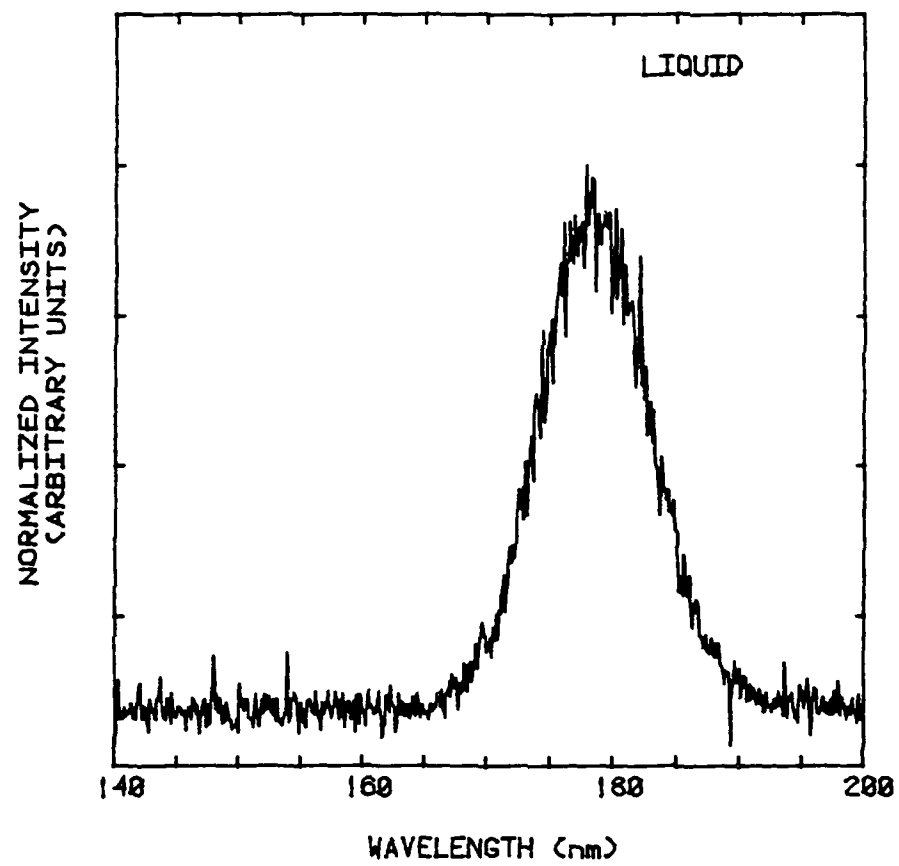


Figure 14. Wavelength Scan of Liquid Xenon.

shown in Figure 3, and coupled to the 172 nm radiation by means of a CaF₂ window. A drawing of the side cell is shown in Figure 15. The cell was evacuated with Valve 1 closed, and a filled LN₂ dewar was placed over the XeF₂ reservoir to allow the XeF₂ to solidify. All remaining gaseous contaminants were pumped away by opening Valve 1 with the LN₂ dewar still in place. The reservoir was then allowed to warm to room temperature while the pressure was monitored with the vacuum pumps shut off. This process was repeated to insure that all impurities were removed from the XeF₂. The chamber was then allowed to remain under an XeF₂ environment (vapor pressure is 4.7 Torr at 293°K) for 24 hours to insure that complete passivation of the chamber had taken place. The system was pumped out a final time just prior to data taking to remove any remaining impurities. Typical results obtained using the UV-V monochromator (Mod. 82-020 in Figure 3) are shown in Figure 16. The Xe pressure in the stainless steel scintillation cell of Figure 3 was 1500 torr and the data in Figure 16 were obtained for a time average beam current of 100 namps. Figure 17 shows an expansion of the wavelength region 280-385 nm from Figure 16. Note the vibrational structure observed in the decay of the XeF (B) state.

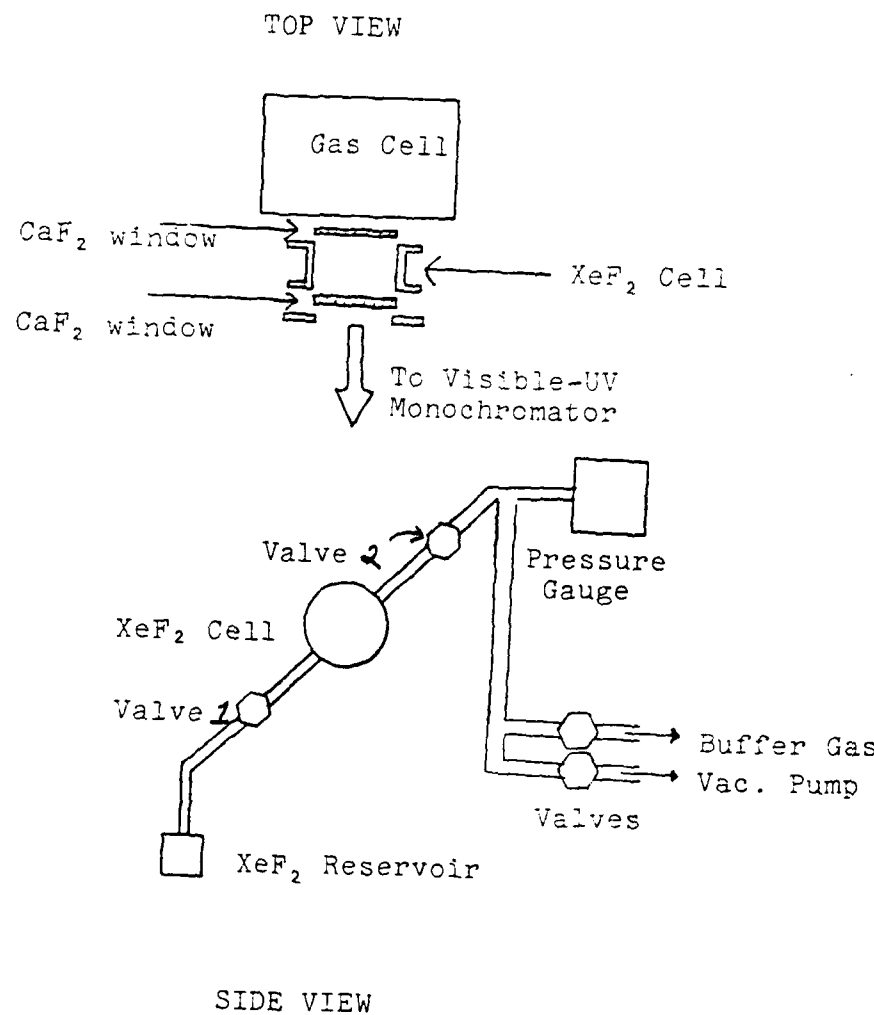


Figure 15. XeF_2 photodissociation cell.

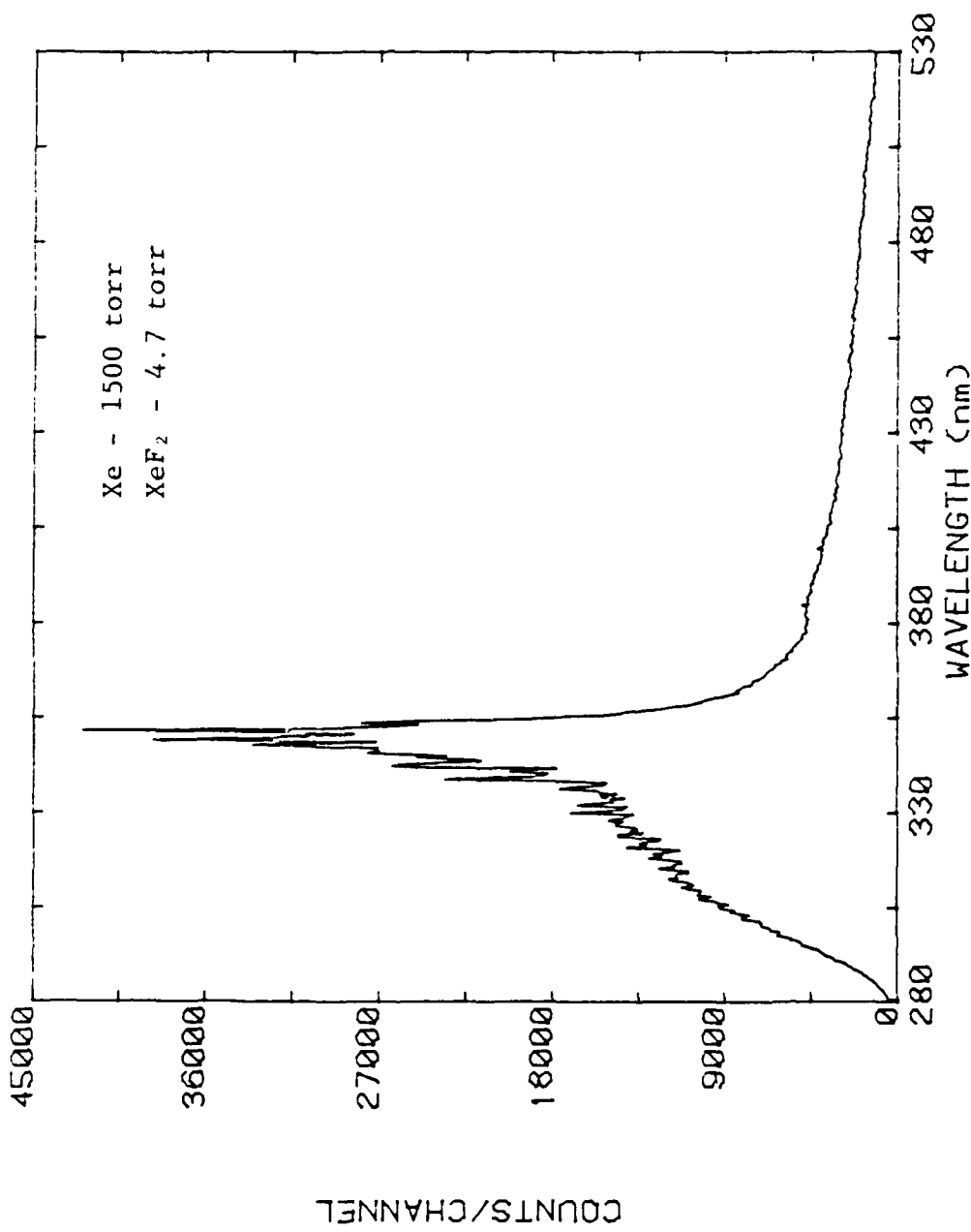


Figure 16. XeF₂ Scan [XeF (B-X) - 351 nm, XeF (C-A) - 483 nm]

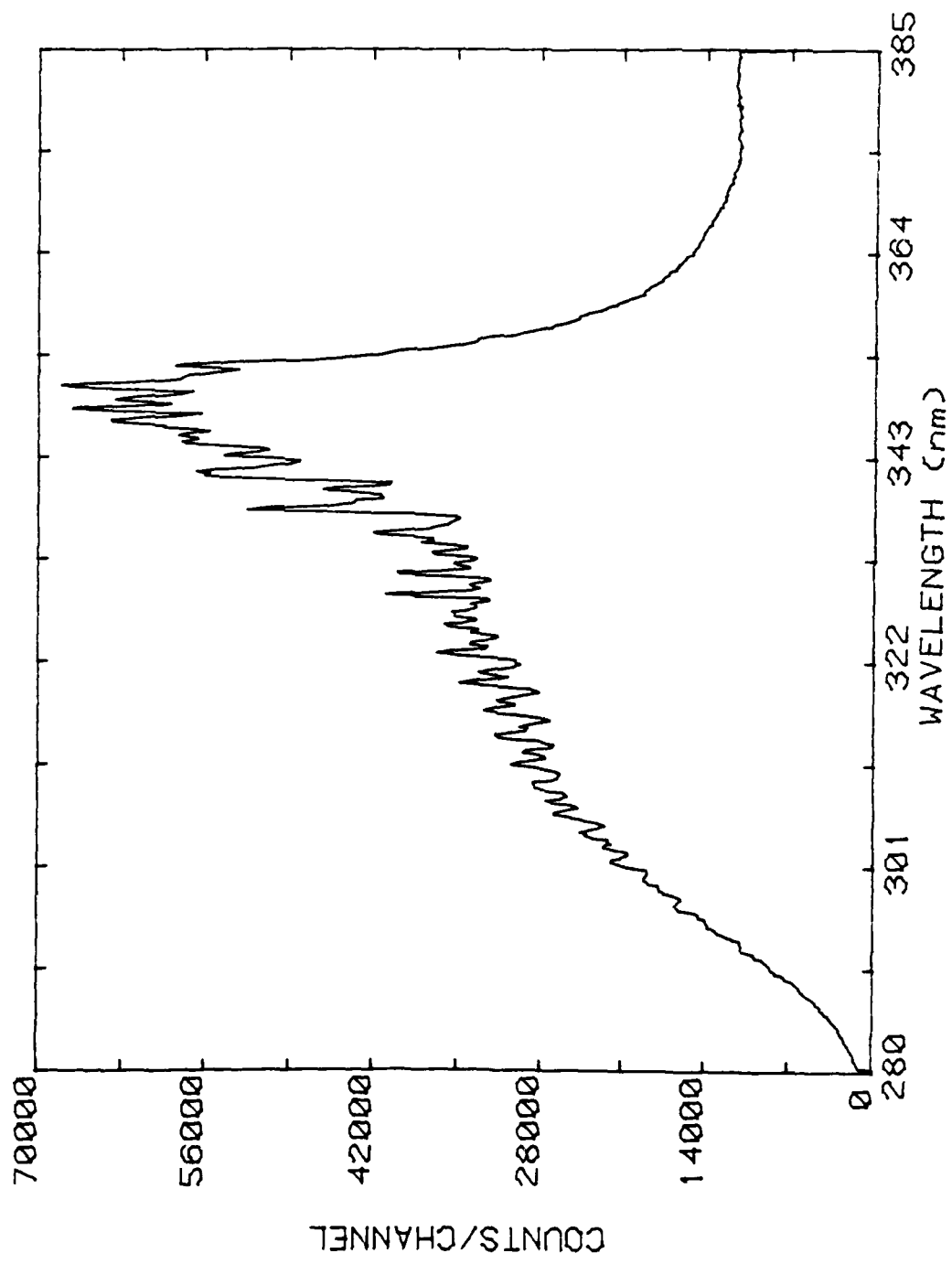


Figure 17. The XeF (B-X) Decay. Note vibrational structure.

III. EXPERIMENTAL RESULTS

Time Resolved Work

Time resolved spectroscopy was performed for the 147 nm resonance line in atomic xenon, the first continuum in Xe_2^* at 152 nm, and the second continuum in Xe_2^* at 172 nm. All time resolved spectra were made at the peak intensity of the particular band studied. This was important in observing the first continuum radiation, but of less importance for the resonance line and the second continuum. The maximum intensity of the first continuum shifted about 5 nm toward the red in the pressure range of 50 Torr to 500 Torr.

Typical time resolved data are given in Figures 7-9. All data taken, at low pressures, could be adequately fit with a two component exponential curve of the form,

$$I(t) = A_1 e^{-\lambda_1 t} + A_2 e^{-\lambda_2 t}$$

where A_1 and A_2 are the amplitudes of the exponentials, while λ_1 and λ_2 are the fast and slow decay rates, respectively. Each wavelength region is discussed below.

First Continuum and Resonance Line

As stated in the introduction, the precursor of the ${}^1\Sigma_u^*$ in Xe_2 is believed to be the 3P_1 resonance state in atomic xenon. To check this hypothesis the decay rate of the resonance line in atomic xenon should be compared to the decay of the first continuum. Since the radiative lifetime of the ${}^1\Sigma_u^*$ state in Xe_2 is only 5 ns³, the decay of the first continuum intensity should have the same pressure dependence as that of the resonance line. Plots of the decay rates as a function of pressure for the resonance line and the first continuum band are shown in Figures 17 and 18, respectively.

The solid lines on Figures 17 and 18 are least square polynomial fits to the data. The solid lines are given by

$$D.F.({}^3P_1) = 1.6 \times 10^5 + 1.5 \times 10^4 P + 61P^2 \quad 1)$$

$$D.F.({}^1\Sigma_u^*) = 2.4 \times 10^5 + 2.7 \times 10^3 P + 62P^2 \quad 2)$$

for the resonance line and the first continuum respectively, where D.F. is the destruction frequency in sec⁻¹ and P is the xenon pressure in Torr. The three body rate constant (P^2 coefficient) is seen to be the same in both cases, within experimental error. The pressure independent term in Eq. 1 is characteristic of radiation trapping of the resonance line, as described by Holstein^{23,24}. The two body terms are discussed in Chapter IV.

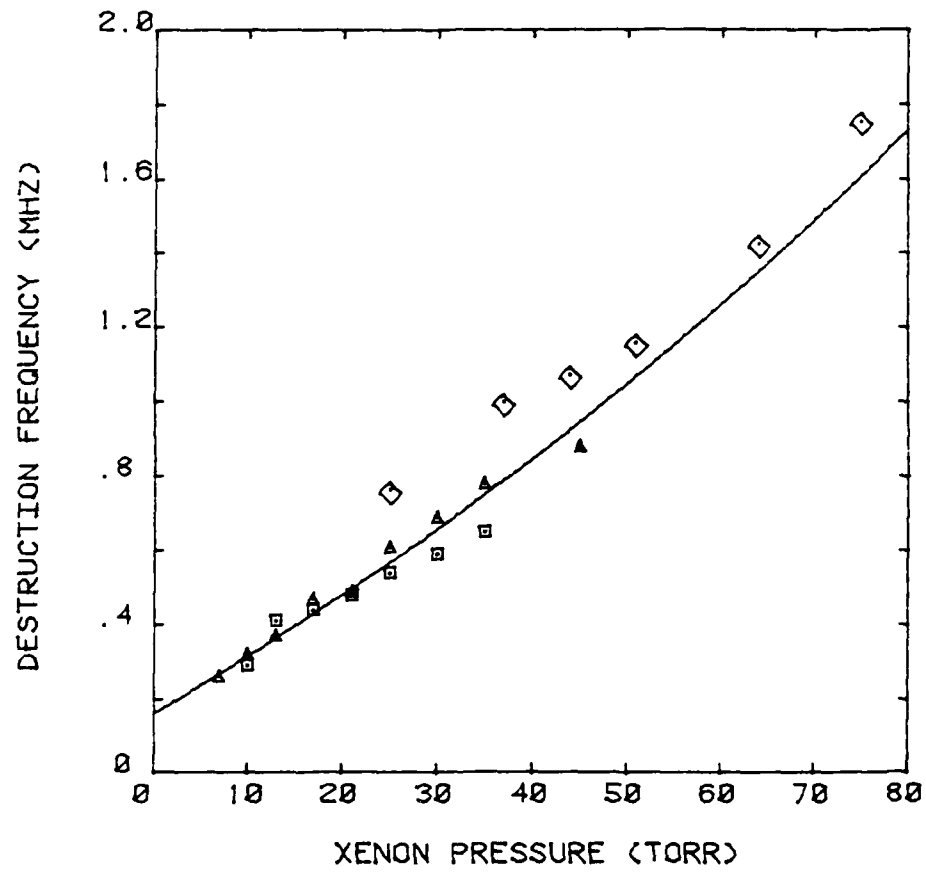


Figure 18. Destruction Frequency vs. Xenon Pressure for the 147 nm Resonance Line. The solid line is a fit to the average of the data shown.

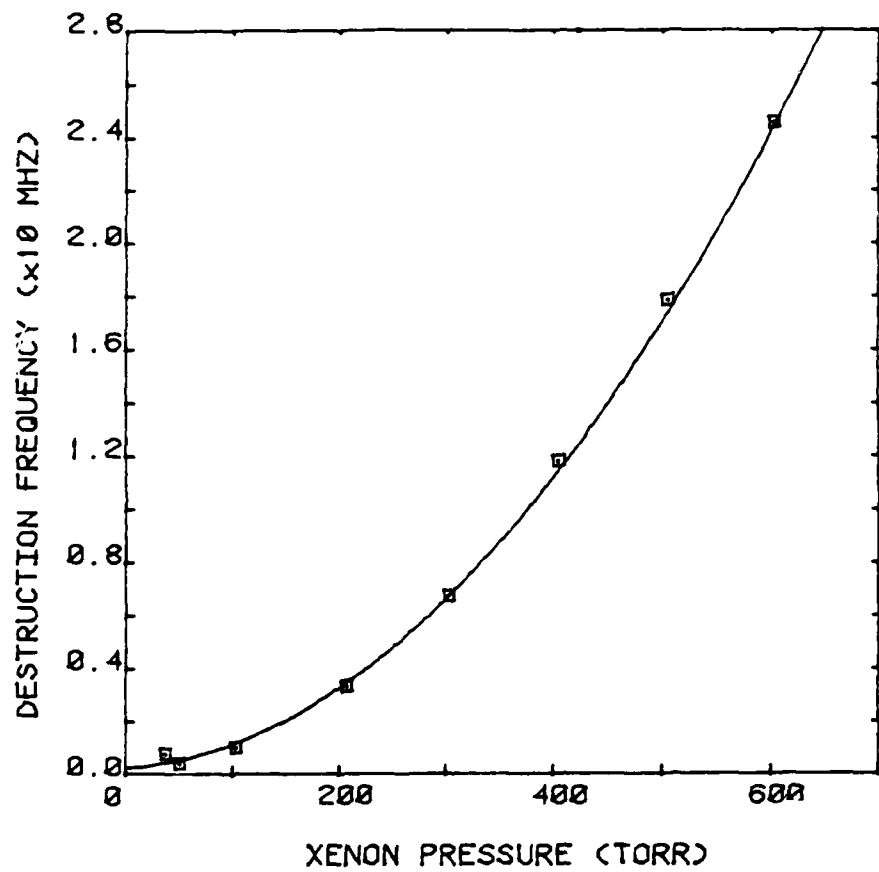


Figure 19. Destruction Frequency vs. Xenon Pressure for the 152 nm First Continuum.

Second Continuum at 172 nm

Data at 172 nm was collected using pressures from 40 Torr to 1200 Torr. Figure 19 shows the pressure dependence of the second continuum below 200 Torr. The solid curve is a least squares fit to the data. The solid curve is given by

$$D.F.({}^3\Sigma_u^-) = 8 \times 10^4 + 3556P + 33P^2 \quad 3)$$

Since the coefficient of the P^2 term is a measure of the three body rate constant for the formation of $Xe_2^*({}^3\Sigma_u^*)$, we see that the P^2 coefficient gives a three body rate constant of $33 \text{ Hz} \cdot \text{Torr}^{-2}$.

The pressure dependence of the second continuum above 200 Torr is shown in Figure 20. Note that for pressures above 600 Torr, the decay rate becomes independent of the pressure. Since this pressure independent rate equals 9.8 MHz, we associate this with the radiative lifetime of 102 ns for the ${}^3\Sigma_u^-$ state of Xe_2^* . The pressure of 600 Torr is a measure of the 'inversion' pressure, where the production rate via three body collisions equals the radiative rate. Since the production is a three body effect, we have

$$KP^2 = \frac{1}{\tau}$$

With $P = 600 \text{ Torr}$ and $\frac{1}{\tau} = 10^7 \text{ Hz}$, we see that $K = 28 \text{ Hz} \cdot \text{Torr}^{-2}$, in agreement with the P^2 coefficient above.

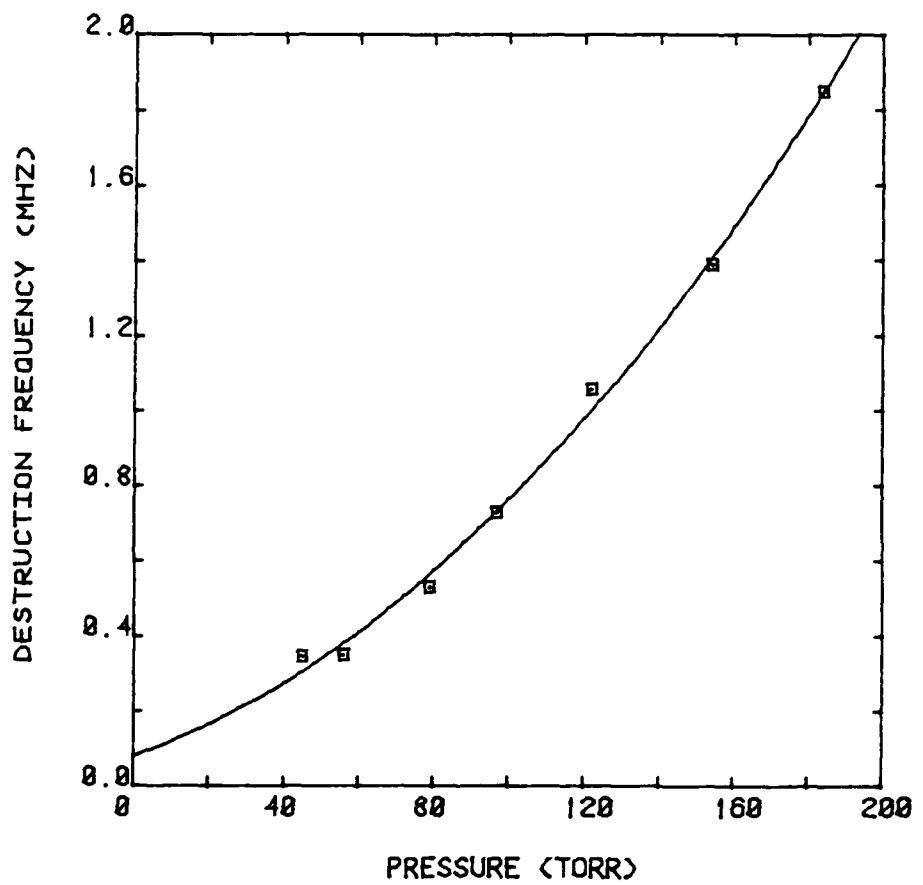


Figure 20. Destruction Frequency vs. Pressure
for the 172 nm Second Continuum.
 $P < 200$ Torr

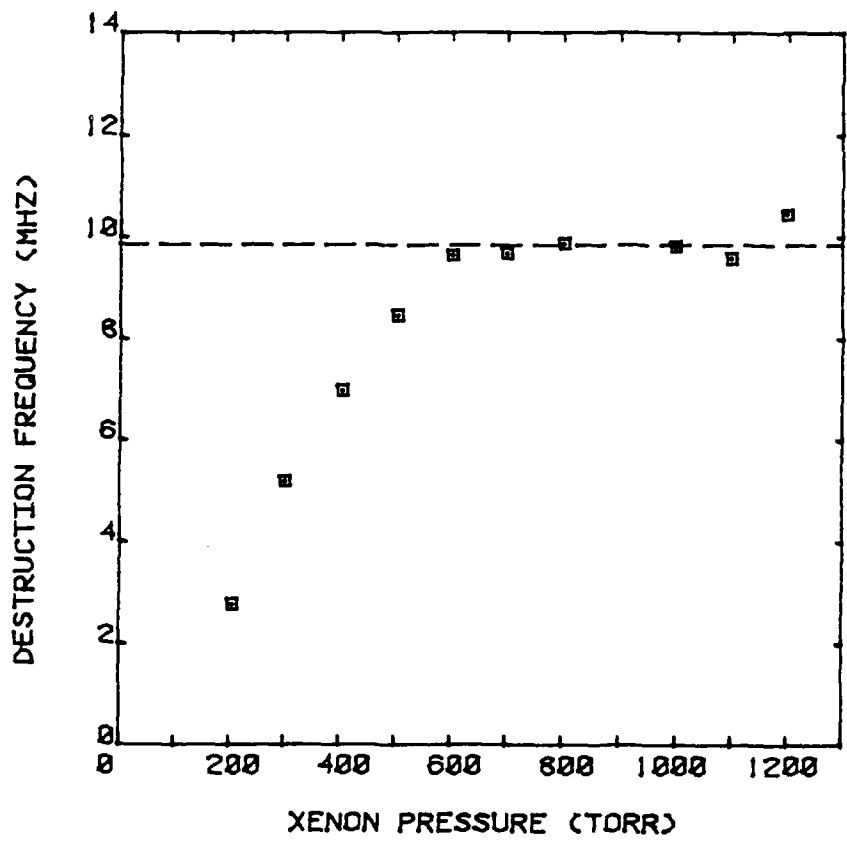


Figure 21. Destruction Frequency vs. Pressure for the 172 nm Second Continuum, $P > 200$ Torr.

Wavelength Resolved Work

Wavelength resolved work was done using the techniques discussed in Chapter II. Scans were taken in 500 Torr increments from 500 Torr to 2500 Torr. This data is plotted in a three dimensional form in Figure 21. Each curve in Figure 21 has been corrected for beam current fluctuations, but not for monochromator efficiency.

The pressure dependence of the light output between 140 and 200 nm is given in Figure 22. Again, this is an arbitrary scale.

In order to perform an absolute intensity measurement, it was necessary to calibrate the monochromator using the technique discussed in Appendix B. Using this technique, the absolute efficiency of the monochromator was measured as a function of wavelength. Finally a scan of the region from 140 nm to 200 nm was made for the proton excited xenon, using an identical setup as that used for the calibration. This beam scan was then used as a normalization point and the data shown in Figure 22 was scaled accordingly. This provided an absolute intensity curve.

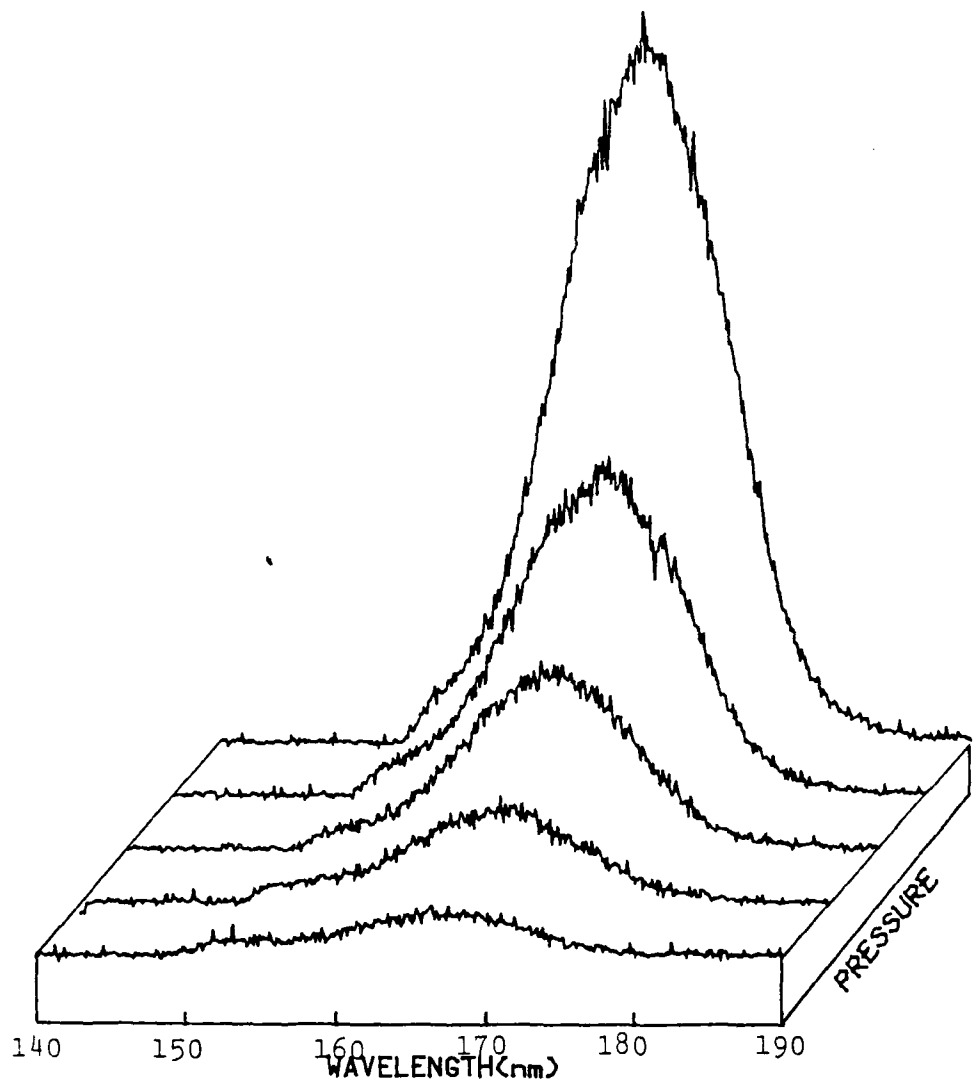


Figure 22. Intensity vs. Pressure vs. Wavelength for xenon scans. Lowest pressure is 500 Torr and the pressure increment is 500 Torr.

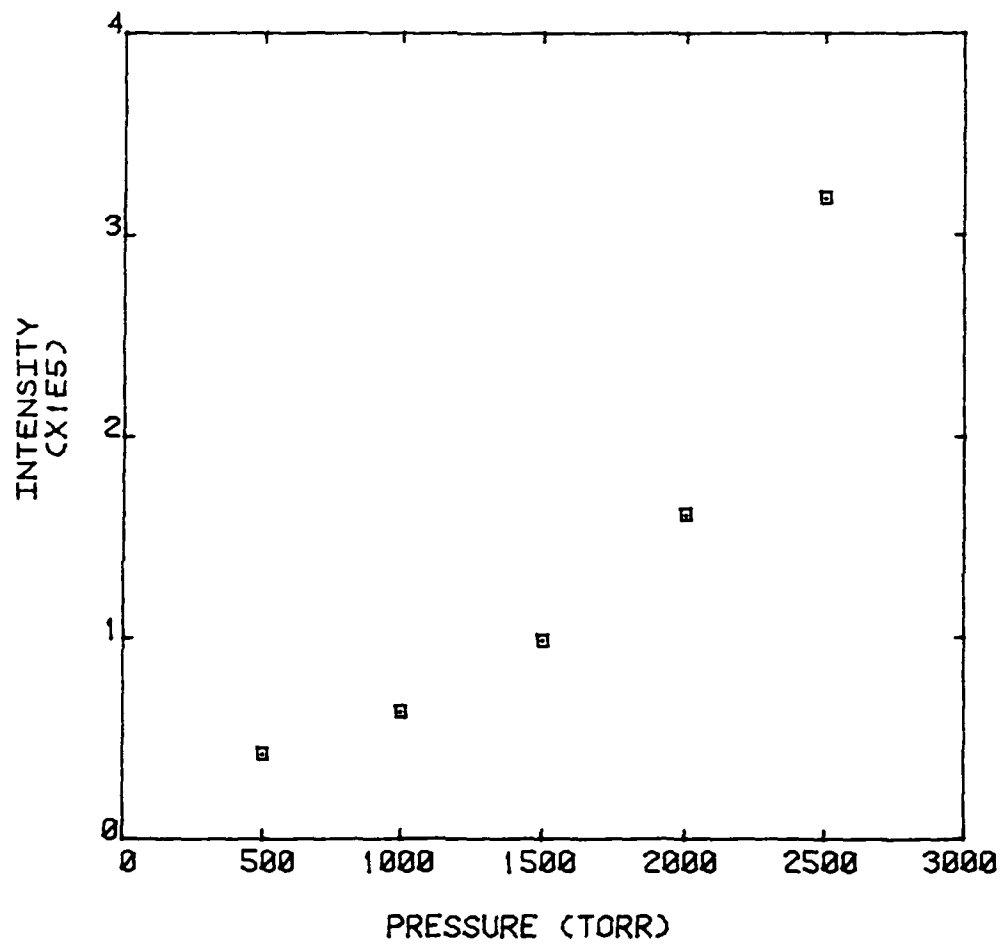


Figure 23. Intensity vs. Pressure for the Wavelength Resolved Scans. This is not corrected for monochromator efficiency.

XeF₂ Photodissociation

Attempts were made to photodissociate XeF₂ using the methods discussed in the previous chapter. Initially a check was made to ensure that the optical thickness of the XeF₂ was sufficient to stop the incident VUV photons from Xe₂^{*}. The standard D₂ lamp, with known output per unit wavelength interval, was used as a source of VUV photons, and these photons were incident on the XeF₂ cell. Two scans were made, first with the cell pumped out to $\sim 10^{-5}$ Torr, and then with the cell at an XeF₂ pressure of 4.7 Torr. The results of these scans were shown in Figure 24, and it is obvious that the VUV photons were absorbed in the XeF₂ cell, particularly in the 160 to 180 nm region, where the intensity of the Xe₂^{*} continuum is a maximum.

Experimental results using Ar as a buffer gas are shown in Figure 25. As indicated the Ar pressure was varied from 0 to 2325 Torr, and each scan in Figure 25 was taken with a time average current of 100 namps and 1500 Torr pure Xe in the stainless steel scintillation cell shown in Figure 3. There is a definite decrease in the B state fluorescence intensity as the Ar pressure is increased; however, no corresponding increase in the C state intensity is observed. In other words we have not been able to collisionally relax the B state population to the C state which lies slightly below

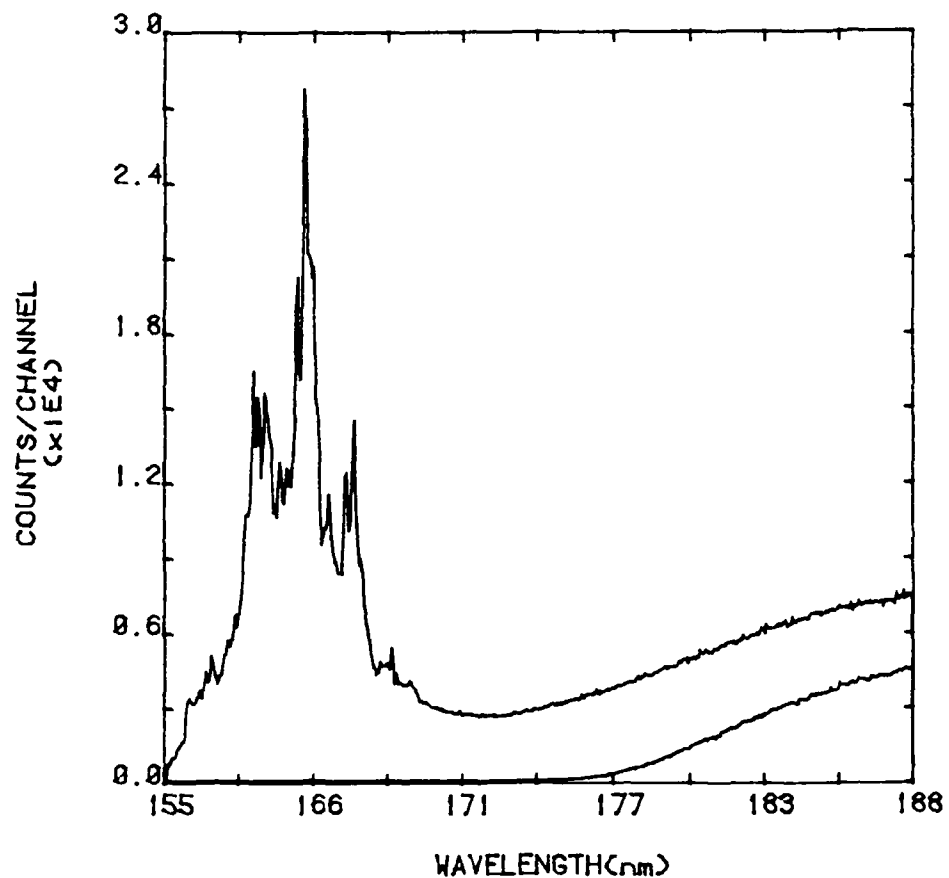


Figure 24. Deuterium Lamp Scan through XeF_2 Cell.
Top scan is through vacuum and the
lower scan is through $\sim 2 \text{ cm } \text{XeF}_2$ at
4.7 Torr.

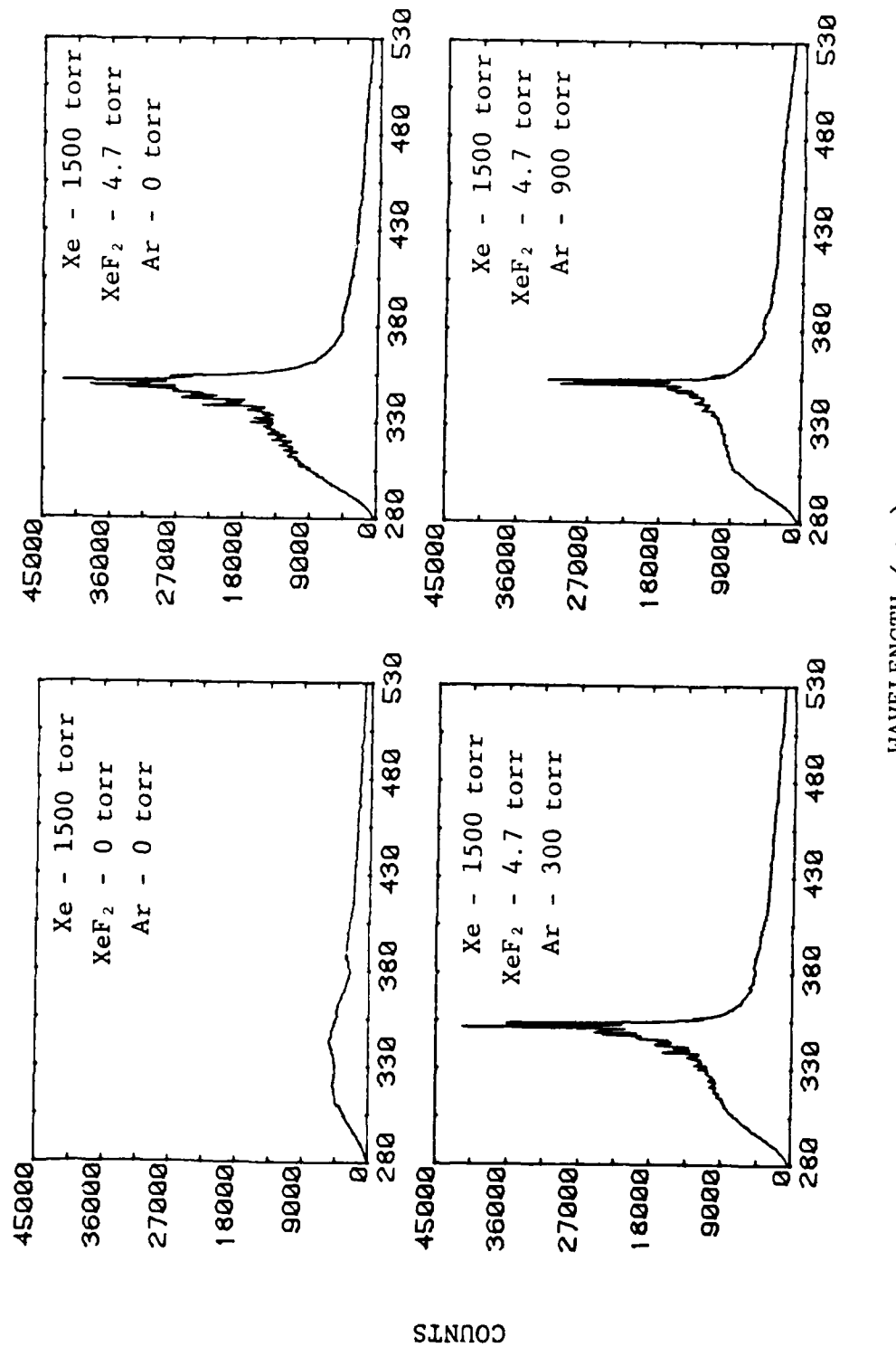


Figure 25. XeF₂ Scans vs. Ar Buffer Gas Pressure. All data taken with
 $P_{Xe} = 1500$ torr and $i_{ave} = 100$ namps.

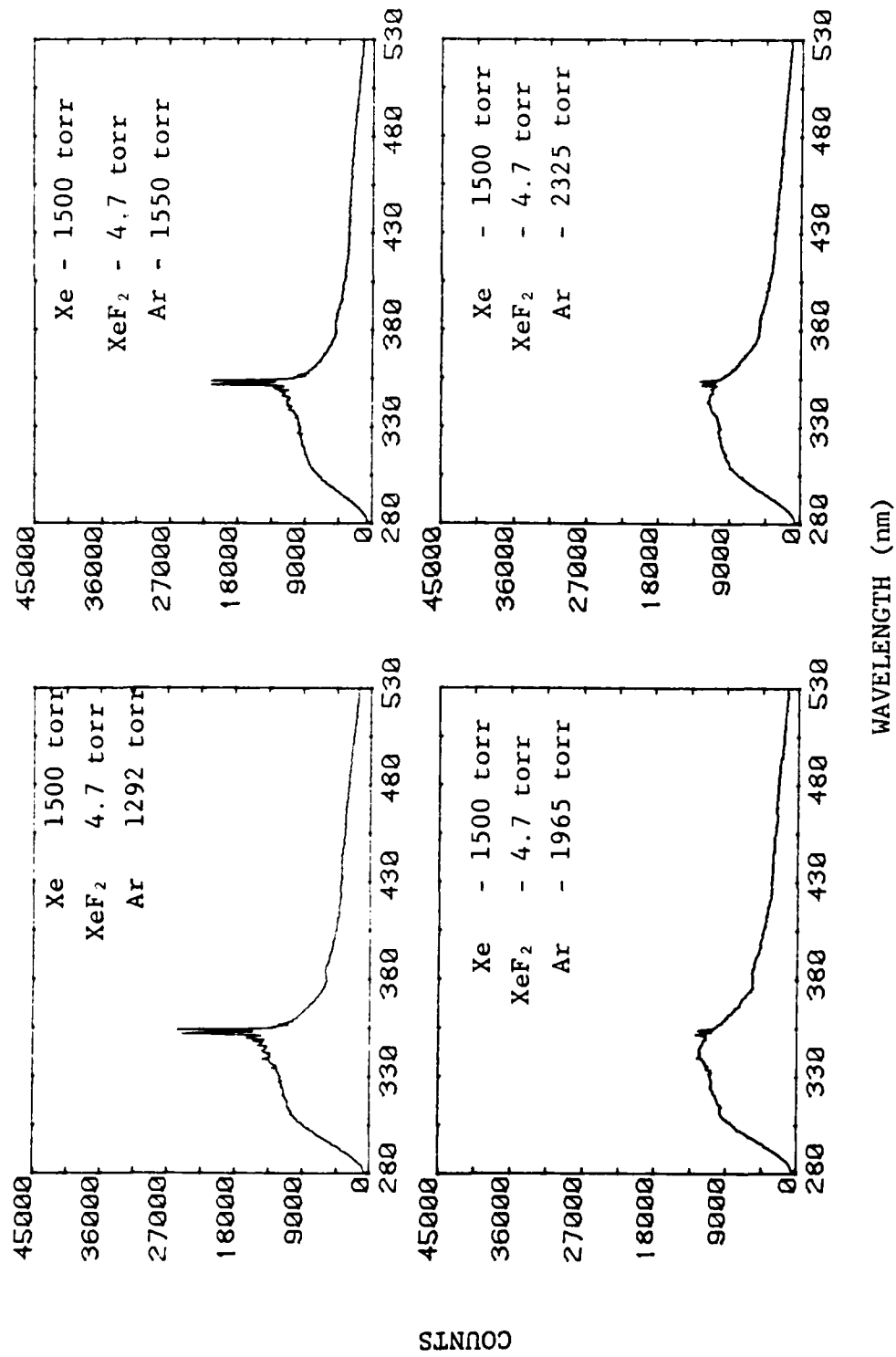


Figure 25 continued. XeF₂ Scans vs. Ar Buffer Gas Pressure. All data taken with P_{Xe} = 1500 torr and i_{ave} = 100 namps.

the B state in energy. We have no satisfactory explanation for this result unless we somehow have not accounted for some residual contaminant in the XeF_2 cell.

Absolute Conversion Efficiency

In conjunction with the absolute emission spectra obtained, it was desired to know the absolute emission efficiency of VUV photon energy output to proton energy deposited in the interaction volume. The energy emitted by VUV photons could be determined by knowing the number of photons emitted at a given wavelength and using the relation

$$E_{\text{emitted}} = hc \sum_{i=1}^N \frac{n_i}{\lambda_i}$$

where

h = Planck's Constant

n_i = number of photons at wavelength λ_i

c = speed of light

The energy deposited in the interaction volume, the volume of the gas cell seen by the VUV monochromator, could be found knowing the number of protons incident upon the gas cell times the energy lost in traversing the interaction length. A computer program was written to calculate the energy loss for a single photon passing the first through the 5.14×10^{-4} cm entrance foil and then through a volume of xenon gas equal to the interaction volume. The computer program is discussed in Appendix A, and all necessary data is given there.

The absolute conversion efficiency is then defined to be the ratio of the emitted energy to the deposited energy, and the conversion efficiency as a function of Xe gas pressure is shown in Figure 25.

Also shown in Figure 25 is the result of an absolute conversion efficiency measurement for liquid Xenon. This measurement was made with the same techniques and procedures used for the gaseous conversion efficiency measurements.

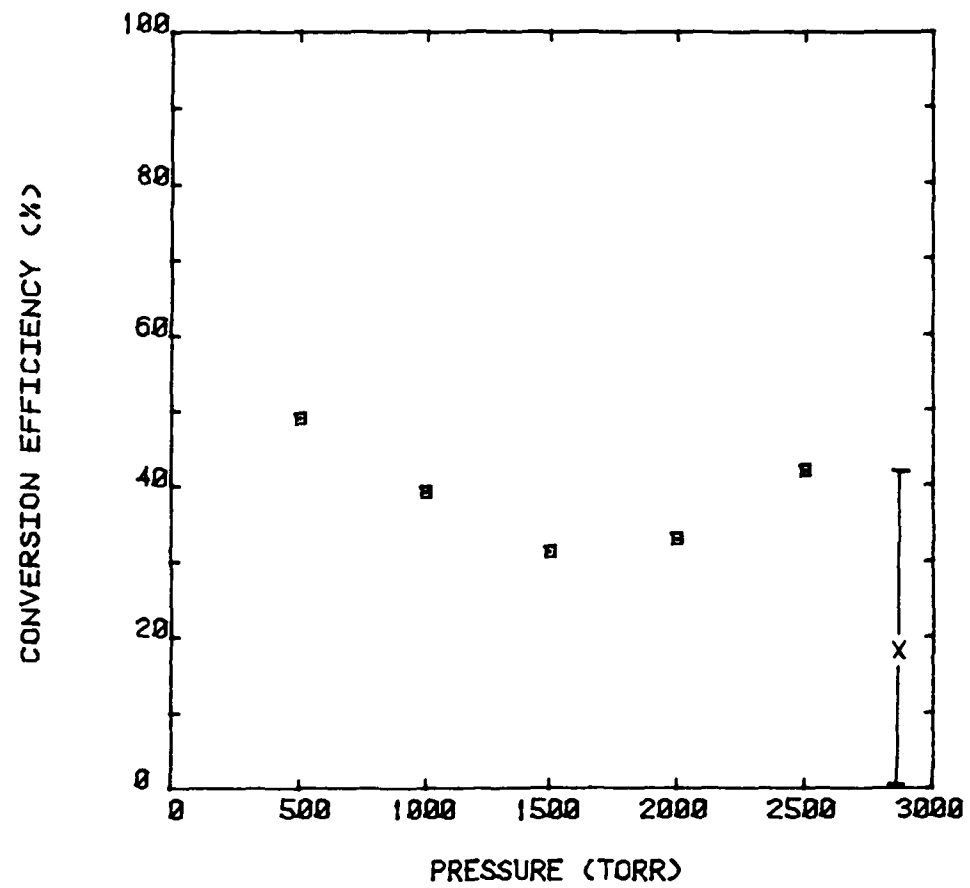


Figure 26. Conversion Efficiency vs. Pressure.
The (X) indicates the result for liquid
Xenon.

IV. KINETIC MODEL

From the experimental data presented in the previous chapter, a kinetic scheme is presented which conforms to this experimental evidence. The pressure dependence of the time behavior of the resonance line, the first continuum, and the second continuum is given below

$$D.F.({}^3P_1) = 1.6 \times 10^5 + 1.5 \times 10^4 P + 61P^2$$

$$D.F.({}^1\Sigma_u^-) = 2.4 \times 10^5 + 2685P + 62P^2$$

$$D.F.({}^3\Sigma_u^-) = 8.0 \times 10^4 + 3556P + 33P^2 \quad P < 200 \text{ Torr}$$

$$D.F.({}^3\Sigma_u^-) = 9.8 \times 10^6 \quad P > 600 \text{ Torr}$$

where D.F. is the destruction frequency of the state in sec^{-1} , and P is the xenon pressure in Torr. Figure 26 illustrates the collisional and radiative processes involved in the kinetics scheme.

As stated in the introduction, mixing of the molecular states has been neglected, as it is due primarily to free electrons. All ion-electron and ion-ion processes are not considered, as we are primarily interested in the excited state channel reactions. Mixing of the molecular states due to collision has not been

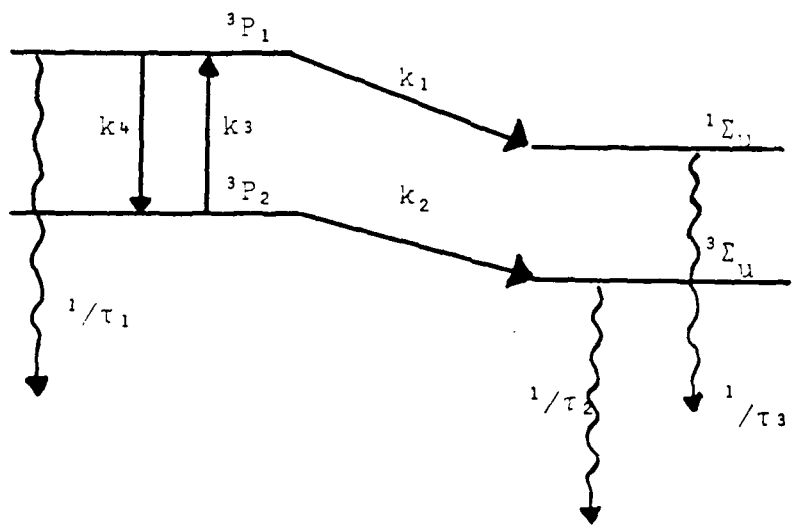
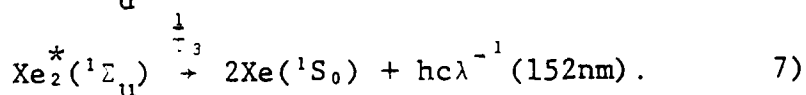
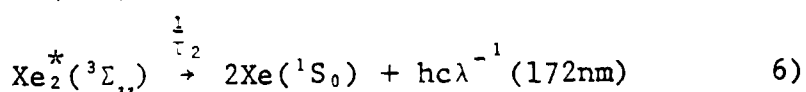
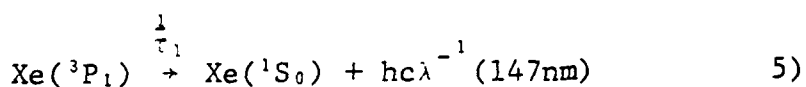
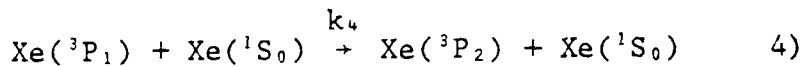
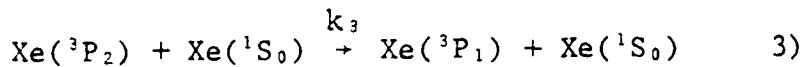
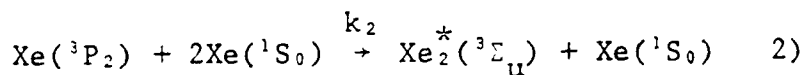
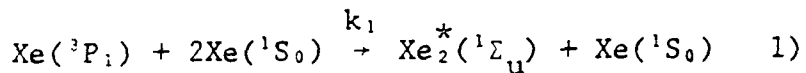


Figure 27. Summary of the collisional and radiative processes in Xe and Xe₂^{*}.

considered, since Keto has shown⁴ these processes to be very slow at the pressures involved in this work.

Using the notation in Figure 26, we can write the reactions involved in the kinetics scheme:



These reactions give rise to a set of differential equations which govern the population of each state. The rate equations are:

$$\frac{dR}{dt} = -k_1 P^2 R - k_4 PR + k_3 PM - \frac{R}{\tau_1} \quad 8)$$

$$\frac{dM}{dt} = -k_2 P^2 M - k_3 PM + k_4 PR \quad 9)$$

$$\frac{dU}{dt} = k_1 P^2 R - \frac{U}{\tau_3} \quad 10)$$

$$\frac{dL}{dt} = k_2 P^2 M - \frac{L}{\tau_2} \quad 11)$$

where

R = population of 3P_1 state

M = population of 3P_2 state

U = population of ${}^1\Sigma_u$ state

L = population of ${}^3\Sigma_u$ state

P = xenon pressure in Torr.

These differential equations are solved in Appendix C,
and the solutions are:

$$R(t) = R_0 [e^{-\lambda_1 t} + e^{-\lambda_2 t}] \quad (12)$$

$$M(t) = \left(\frac{k_4 P R_0}{\lambda_1 - \lambda_2} + k_4 P R_0 t + M_0 \right) e^{-\lambda_2 t} - \frac{k_4 P R_0}{\lambda_2 - \lambda_1} e^{-\lambda_1 t} \quad (13)$$

$$U(t) = \frac{k_1 P^2 R_0}{\lambda_1 - \frac{1}{\tau_3}} e^{-\lambda_1 t} + \frac{k_1 P^2 R_0}{\lambda_2 - \frac{1}{\tau_3}} e^{-\lambda_2 t} + \left(\frac{k_1 P^2 R_0}{\lambda_1 - \frac{1}{\tau_3}} - \frac{k_1 P^2 R_0}{\lambda_2 - \frac{1}{\tau_3}} \right) e^{-\frac{t}{\tau_3}} \quad (14)$$

$$L(t) = \frac{k_2 P^2 D'}{\lambda_1 - \frac{1}{\tau_2}} e^{-\lambda_1 t} - \frac{k_2 P^2 D}{\lambda_2 - \frac{1}{\tau_2}} e^{-\lambda_2 t} + \left(\frac{k_2 P^2 D}{\lambda_2 - \frac{1}{\tau_2}} - \frac{k_2 P^2 D'}{\lambda_1 - \frac{1}{\tau_2}} \right) e^{-\frac{t}{\tau_2}} \quad (15)$$

where λ_1 , λ_2 , D , D' , R_0 and M_0 are defined as follows;

$$\lambda_1 = k_1 P^2 + k_4 P + \frac{1}{\tau_1}$$

$$\lambda_2 = k_2 P^2 + k_3 P$$

$$D = \frac{k_4 P R_0}{\lambda_1 - \lambda_2} + k_4 R_0 P t + M_0$$

$$D' = \frac{k_4 P R_0}{\lambda_2 - \lambda_1}$$

R_0 = initial resonance state population

M_0 = initial metastable state population.

The 3P_1 resonance state population is governed by Eq. 12 and is seen to be a two component exponential. In the pressure range less than 100 Torr, $\lambda_1 > \lambda_2$, so the fast decay, when plotted as a function of xenon pressure, should have a quadratic dependence. This indeed was the case as was shown in Figure 17. The coefficients of each term give us the reaction rate constant, as was discussed in Chapter III.

The first continuum pressure dependence was shown in Figure 18 and we saw that the P^2 coefficient was essentially the same as that for the 3P_1 resonance state. This is intuitively obvious when one considers the 3P_1 state as the precursor of the $^1\Sigma_u$ state via three body collisions. The radiative lifetime of the $^1\Sigma_u$ state has been measured³ to be on the order of 5 ns, so that as soon as the 3P_1 atom collides with two ground state atoms to form the $^1\Sigma_u$ molecule, the molecule radiates. There is no problem encountered with the production rate of the $^1\Sigma_u$ molecule equalling the radiative rate, since the radiative lifetime is so short. We can therefore conclude that decays from the $^1\Sigma_u$ molecule occur from high vibrational levels, as the molecule does not have time to relax vibrationally before radiating. The lack of agreement between the two body rate constants is not well understood. At best, the P coefficients give limits for the two body rate constants.

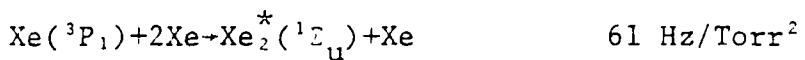
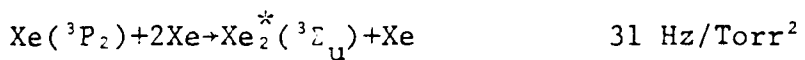
If we now look at Eqs. 12 and 14, we see that the first terms in both equations have the same exponential time dependence, and hence the same pressure dependence by the definition of λ_1 . The second term of Eq. 12 comes about by upward mixing of the 3P_2 state to the 3P_1 state. Since this process is not energetically favorable, we expect the second term to be suppressed with respect to the first term. The second term in Eq. 14, which also comes about by upward mixing of the 3P_2 state with the 3P_1 state, simply reflects this and is therefore not seen in the experiment. The last term in Eq. 14 is the production rate of the $^1\Sigma_u^-$ molecule. The $e^{-\frac{t}{\tau_3}}$ factor is very small, even at very short times, and not resolved in this work.

Turning now to the $^3\Sigma_u^-$ state, we consider Eqs. 13 and 15. As mentioned earlier, the 3P_2 atom does not²⁵ radiate to the ground state by dipole radiation, hence its presence is not observed directly in these experiments. We can, however, determine the three body rate constant for the formation of the $^3\Sigma_u^-$ molecule by observing the pressure dependence of the decay of the $^3\Sigma_u^-$ molecule. Unlike the $^1\Sigma_u^-$ molecule, the $^3\Sigma_u^-$ molecule has a rather long radiative lifetime, measured in this work to be 102 ns. Hence the difference denominators will come into play in Eq. 15. We first note that the first term in

Eq. 15 is a result of the mixing of the 3P_1 state into the 3P_2 state, which is energetically favored in the downward transition. The second term comes about due to the three body collisions of the 3P_2 atoms with ground state atoms, giving rise to the formation of the $^3\Sigma_u$ molecule. We see also that the third term in Eq. 15 is the radiative lifetime term.

We must consider two possible cases, when $\lambda_2 > \frac{1}{\tau_2}$ and $\lambda_2 < \frac{1}{\tau_2}$. When $\lambda_2 > \frac{1}{\tau_2}$, the second term in Eq. 15 represents the production rate of the $^3\Sigma_u$ molecule while the third term represents the decay rate. When $\lambda_2 < \frac{1}{\tau_2}$, the converse is true. Only the decay rate of the $^3\Sigma_u$ molecule was quantitatively observed in this work, so we should see the decay rate become independent of the pressure when the second term changes sign. This was indeed observed, as shown in Figure 20. The inversion pressure can then be used to measure the three body rate constant, as was done in Chapter III. If one were to look at the production rate of the $^3\Sigma_u$ molecule at pressures lower than the inversion pressure, it should be independent of the pressure. In the same light, the decay rate below the inversion pressure should have a pressure dependence given by λ_2 . This again is the case, as was shown in Figure 19. The agreement between the rate constants measured in this manner tends to support the kinetic

scheme outlined above. The production rate below the inversion pressure was observed qualitatively and was seen to be pressure independent. The results of this work are summarized below.



The lifetime of the ${}^3\Sigma_u^+$ state is in excellent agreement with the work of Leichner⁹ and Keto³. The ${}^1\Sigma_u^+$ three body rate constant is larger than that measured by Leichner⁹, and considerably lower than that measured by Timpson and Anderson⁵. The lack of agreement with Leichner not well understood, as the experimental technique is quite similar, however the two independent determinations of the three body rate constant from the atomic metastable state supports the inversion pressure measurement. This second check was not performed by Leichner.

V. DISCUSSION AND SUMMARY

Kinetics and Time Resolved Work

The kinetic model developed in the preceding chapter incorporates all experimental facts. The lack of agreement in the atomic mixing terms cannot be explained fully, however the three body reaction rates agree remarkably well. A similar kinetic scheme has been presented by Leichner⁹, and a less complete one was presented by Millet⁸. The two body downward mixing rate constant found here is larger than that found by Leichner, as are the three body rates. Millet did not see any two body effects at all, which is surprising for the pressure range in which he worked.

The experimental results show that the 3P_1 and 3P_2 atomic states are the precursors of the $^1\Sigma_u^*$ and $^3\Sigma_u^*$ molecular states respectively, through three body collisions. This was tacitly assumed in the beginning and was borne out by the experiment.

Wavelength Resolved Work

The emission spectra of the $Xe-Xe_2^*$ system was found to consist of the 3P_1 atomic transition, the $^1\Sigma_u^*$

molecular band centered at 152 nm, and the $^3\Sigma_u^-$ molecular band centered at 172 nm. The second continuum at 172 nm was found to have an essentially gaussian profile, as expected from a vibrationally relaxed system. The first continuum at 152 nm began just after the 3P_1 resonance line and extended into the wings of the second continuum. All spectra were similar to those observed by others.

The emissions from liquid xenon consisted only of the second continuum, no resonance line or first continuum was observed. This is to be expected, as the density of atoms is much greater, and hence the equivalent pressure much higher than in the gaseous systems. The three body reaction from the 3P_2 metastable state will dominate the kinetics at liquid densities, hence only the second continuum will be observed.

The second continuum in liquid xenon was seen to be shifted toward the red by 5 nm. This shift was noted in all liquid scans and was very reproducible. While a complete explanation cannot be offered, the local potential seen by a molecule has been shifted downward. This is equivalent to the internuclear separation becoming smaller, so that the lower part of the potential well shown in Fig. 1 is closer to the repulsive ground state. While this seems reasonable, it does not preclude an alternative explanation.

Estimation of Error

Data taken at 152 nm and 172 nm repeated quite well on a day to day basis. All data taken was repeated on at least three separate occasions, with a minimum of one day between runs. Care was taken to insure that the xenon flow rate was identical for each run, and the time averaged beam current was set to the same value for each run. The data shown in Figures 19 and 20 are the averaged over all data taken. With these precautions, the time resolved data for the 152 nm and 172 nm band repeated to within $\pm 10\%$ at the 1σ confidence level. The error from day to day was determined by comparing the destruction frequency at a given xenon pressure obtained on different days. The time resolved data was fit using a multiple linear regression curve fitting routine based on the Marquardt algorithm²¹, as discussed by Bevington²⁸. The program determined the amplitudes and decay constants for the multiple exponential decay, and assigned the 1σ error associated with each parameter. The worst case fit was found to be 9%.

The polynomial fit to these destruction frequencies (each frequency having been assigned an experimental error of $\pm 10\%$) was performed using a least squares fitting routine and the error in the polynomial fit

at the 1σ confidence level was 10% for the data shown in Figure 18 and 13% for the data shown in Figure 19. Using these numbers, the three body rate constant for the formation of the ${}^1\Sigma_u$ state is $61 \pm 8 \text{ Hz}\cdot\text{Torr}^{-2}$ and the three body rate constant for the formation of the ${}^3\Sigma_u$ state is $33 \pm 5 \text{ Hz}\cdot\text{Torr}^{-2}$.

The resonance line data did not repeat nearly as well as the first or second continuum as can be seen in Figure 17. All data taken for the resonance line is shown in Figure 17, and it is evident that the data did not repeat well on a day to day basis at higher pressures. This can be understood from the decrease in intensity of the 147 nm resonance line with increasing xenon pressure. As seen in Figure 17, the data repeated no better than $\pm 20\%$ from the average value at each xenon pressure. The solid line on Figure 17 is shown simply to illustrate that the three body term obtained from the first continuum pressure dependance will fit the resonance line data, within the $\pm 20\%$ quoted above.

Absolute intensity measurements at any wavelength are inherently difficult to perform, particularly in the VUV. No standard continuum source of photons is readily available below 170 nm, precisely the region where this work was performed. As a consequence, it was necessary to rely on the molecular bands of D₂.

As seen in Appendix B, these molecular bands are quite intense, and filters must be used to attenuate the light. If this were not done, the count rate on the PMT and in the main amplifier would quickly exceed the maximum allowed values as stated by the manufacturers. When this occurs, the number of photons counted is considerably less than that detected due to the pile up problem associated with the amplifiers. So we see that the difficulties encountered in this type of measurement are numerous, and as a consequence, the error associated in this type of measurement is greater than in a relative measurement.

Let us assume that the conversion efficiency is actually independent of pressure. This is a reasonable assumption if we recall that fluorescent radiation from the 3P_1 atomic state is not observed at pressures greater than 100 Torr. The curvature seen in Figure 25 is then due to statistical fluctuation around an average value of 41%, and the error assigned to the conversion efficiency is $\pm 23\%$ relative to the absolute conversion efficiency. With this error assignment the average value of 41% from Figure 25 is in fair agreement with a previously measured value²⁶. The same error assignment of $\pm 23\%$ has also been made for the liquid Xenon point shown in Figure 25.

LIST OF REFERENCES

1. M. McLusker, Topics in Applied Physics, (Springer-Verlog, New York, 1979, Vol. 30.)
2. L. Colli, Phys. Rev., 95, 892, (1954)
3. J. W. Keto, Phys. Rev. Lett., 33, 1365, (1974)
4. J. W. Keto et. al., Chem. Phys. Lett., 42, 125, (1976)
5. P. R. Timpson and J. M. Anderson, Can. Jour. Phys., 42, 1817, (1970)
6. A. W. Geraldo and J. B. Johnson, J. Chem. Phys., 59, 1738, (1973)
7. R. Boucique and P. Mortier, J. Phys. D., 3, 1905, (1970)
8. P. Millet et. al., J. Chem. Phys., 69, 92, (1978)
9. P. Leichner et. al., Phys. Rev. A., 13, 1767, (1976)
10. R. Mullikan, J. Chem. Phys., 52, 5170, (1970)
11. W. Ermler et. al., J. Chem. Phys., 69, 976, (1976)
12. M. Ghelfenstein et. al., Chem. Phys. Lett., 49, 312, (1977)
13. O. Dutuit et. al., Chem. Phys. Lett., 58, 16, (1978)
14. G. Thornton et. al., J. Chem. Phys., 71, 133, (1979)
15. H. Anderson and J. Ziegler, Stopping Powers and Ranges in All Elements, (Pergamon Press, New York)
16. L. C. Northcliffe and R. F. Schilling, Nuclear Data Tables, A7, 233, (1970)

17. E. R. Fisher, Final Technical Report, USABMD Advanced Technology Center, Contract #DASG60-78-c-0055, (1979)
18. T. G. Miller et. al., Rev. Sci. Instrum., 50, 1013, (1979)
19. R. C. Harper, private communication.
20. E. Güldü, Wayne State Univ. Detroit, MI, private comm.
21. D. W. Marquardt, J. Soc. Ind. Appl. Math., 11, 431, (1963)
22. NBS publication number 443.
23. T. Holstein, Phys. Rev., 72, 1212, (1947)
24. T. Holstein, Phys. Rev., 83, 1159, (1951)
25. Enge, Wehr, and Richards, Introduction to Atomic Physics, (Addison Wesley, Mass. 1972)
26. W. M. Hughes et. al., Los Alamos Technical Report (1978)
27. M. Monahan, M. S. Thesis, Auburn Univ., 1979
28. P. Bevington, Data Reduction and Error Analysis for the Physical Sciences, (McGraw-Hill, New York, 1969)

APPENDIX A

ENERGY LOSS CALCULATIONS
FOR PROTONS ON HAVAR
AND XENON

In order to determine the energy deposited in the xenon gas by the proton beam, it is necessary to calculate the energy loss per unit path length as the beam traverses the entrance foil and the length of gas seen by the monochromator. A computer program was written to perform these calculations. The program is written in BASIC, and was designed to run on a Tektronix 4051 mini-computer.

The prescription used was to take the functional form of the dE/dx curve of Ziegler and Anderson¹⁵, and integrate the curve as the particle traversed a given thickness of foil or gas. This energy was then subtracted from the incident energy and the next step was taken until the particle had exited the foil and had traveled the length of gas seen by the monochromator.

The program is included in this appendix. DATA statements 170-220 were taken from Ziegler and Anderson and are the values for HAVAR. The elemental composition of HAVAR is given in Table 2. Line 250 is the initial proton energy before entering the foil. Line 260 steps the beam through the foil. The right endpoint in line 260 is the foil thickness in microns and the stepsize is in microns. Line 270-320 calculate dE/dx

TABLE 2
 Elemental Composition of HAVAR
 and dE/dx coefficients

<i>z</i>	Symbol	wt. fraction	A	B	C	D
						$\times 10^{-2}$
4	Be	.0004	2.592	966	153.8	3.475
6	C	.02	2.989	1445	957.2	2.819
24	Cr	.20	4.489	5616	1336	.8413
25	Mn	.016	3.907	5725	1461	.8829
26	Fe	.1606	3.963	6065	1243	.7782
27	Co	.425	3.535	6288	1372	.7361
28	Ni	.13	4.004	6205	555.1	.8763
42	Mo	.02	7.248	9545	480.2	.5367
74	W	.028	5.144	15930	442.4	.3144

for each element of the HAVAR foil and 330 adds it up to give ΔE for the entire foil. This energy is subtracted from the initial energy in line 340 and checks are made if $E < 0$. Upon completion of the foil loop in line 370, the energy of the beam is printed and the xenon pressure is entered.

The above procedure is repeated for xenon in 530-620. Here the right endpoint is the total distance covered by the monochromator view, and its dimensions are in mm. Final results are printed in line 640.

```
100 REM THIS IS A PROGRAM THE ENERGY LOSS OF PROTONS
    GOING THROUGH
110 REM A HAVAR FOIL. THE THICKNESS OF THE FOIL IS THE
    RIGHT ENDPOINT
120 REM NECESSARY DATA WAS TAKEN FROM ZIEGLER AND ANDERSON
    HYDROGEN
130 REM STOPPING POWER AND RANGES.
140 INIT
150 PAGE
160 DIM A(9),B(9),C(9),D(9),F(9),G(9),H(9)
170 DATA 2.592,2.989,4.489,3.907,3.963,3.535,4.004,7.248,
    5.114
180 DATA 966,1445,5616,5725,6065,6288,6205,9545,15930
190 DATA 153.8,957.2,1336,1461,1243,1372,555.1,480.2,442.1
200 DATA 33.75,28.19,8.413,8.829,7.782,7.361,8.763,5.367,
    3.114
210 DATA 4.05-4,0.02,0.2,0.016,0.1606,0.425,0.13,0.02,0.028
220 DATA 12.05,11.36,8.331,8.15,8.483,8.99,9.126,6.407,6.32
230 READ A,B,C,D,F,G
240 D=D*1.0E-3
250 E=2750
260 FOR J=0 TO 5 STEP 1
270 FOR I=1 TO 9
280 DEF FNA(E)=A(I)*E^0.45
290 DEF FNB(E)=B(I)/E*LOG(1+C(I)/E+D(I)*E)
300 DEF FNC(E)=FNA(E)*FNB(E)/(FNA(E)+FNB(E))
310 H(I)=FNC(E)*F(I)*G(I)
320 NEXT I
330 S=SUM(H)*1
340 E=E-S
350 IF E<=0 THEN 380
360 NEXT J
370 GO TO 400
380 PRINT "E<=0";J
390 GO TO 380
400 PRINT USING 420 E 1000;
410 E1=E
420 IMAGE "ENERGY AFTER BEAM PASSES THROUGH FOIL",1D.3D,
    "MEV"
430 PRINT "JJINPUT PRESSURE OF XENON IN TORR";
440 INPUT P
450 E=E1
```

```
460 A1=9.289
470 B1=12030
480 C1=397.3
490 D1=0.004384
500 DEF FND(E)=A1*E^0.45
510 DEF FNE(E)=B1/E*LOG(1+C1/E+D1*E)
520 DEF FNF(E)=FND(E)*FNE(E)/(FND(E)+FNE(E))*1.0E-15
530 Z=0
540 Z1=0
550 REM UNITS IN LINE 610 ARE KEV PER .1MM
560 REM RIGHT ENDPOINT IS LENGTH OF BEAM PATH SEEN BY
      MONOCHROMETER
570 REM IN MM.
580 FOR J=0 TO 14.2 STEP 0.1
590 Z1=FNF(E)*P*3.21E+16*1.0E-3*0.01
600 Z=Z+Z1
610 E=E-Z1
620 NEXT J
630 PRINT USING 640 Z
640 IMAGE "ENERGY DEPOSITED IN XENON =",4D.2D,"KEV."
650 PRINT "ANOTHER PRESSURE?";
660 INPUT A$
670 FOR I=1 TO 3
680 B$=SEG(A$,I,1)
690 IF B$="Y" THEN 430
700 END
```

APPENDIX B
CALIBRATION PROCEDURES FOR ABSOLUTE
INTENSITY MEASUREMENTS

The monochromator and electronics systems were calibrated using a D₂ lamp manufactured by Hamamatsu TV Company. This lamp was calibrated at 50 cm by the National Bureau of Standards. The calibration conditions are described in the NBS report of calibration and are summarized below.

The lamp was set up 50 cm in front of the entrance slit of the monochromator, whose entrance and exit slits were set to 130 μm by 1 mm. This slit width was chosen to give a band width of 4.2 Å at 170 nm. The lamp was operated at a DC current of 300 mA in an argon atmosphere. The argon was flowed through the gas cell and an interconnecting tube to the lamp at a flowrate of 20 liters per minute. The calibration setup is shown in Figure 27.

The calibration data presented by NBS is given in Table 3. Note that the data given by NBS is in Watts·cm⁻³. This has been converted to photons·cm⁻²·sec⁻¹·nm⁻¹ by the formula,

$$\frac{\text{flux}}{\text{nm}} = 5.03 \times 10^8 \cdot \lambda \cdot P$$

where

λ = wavelength in nm

P = power density in Watts·cm⁻³.

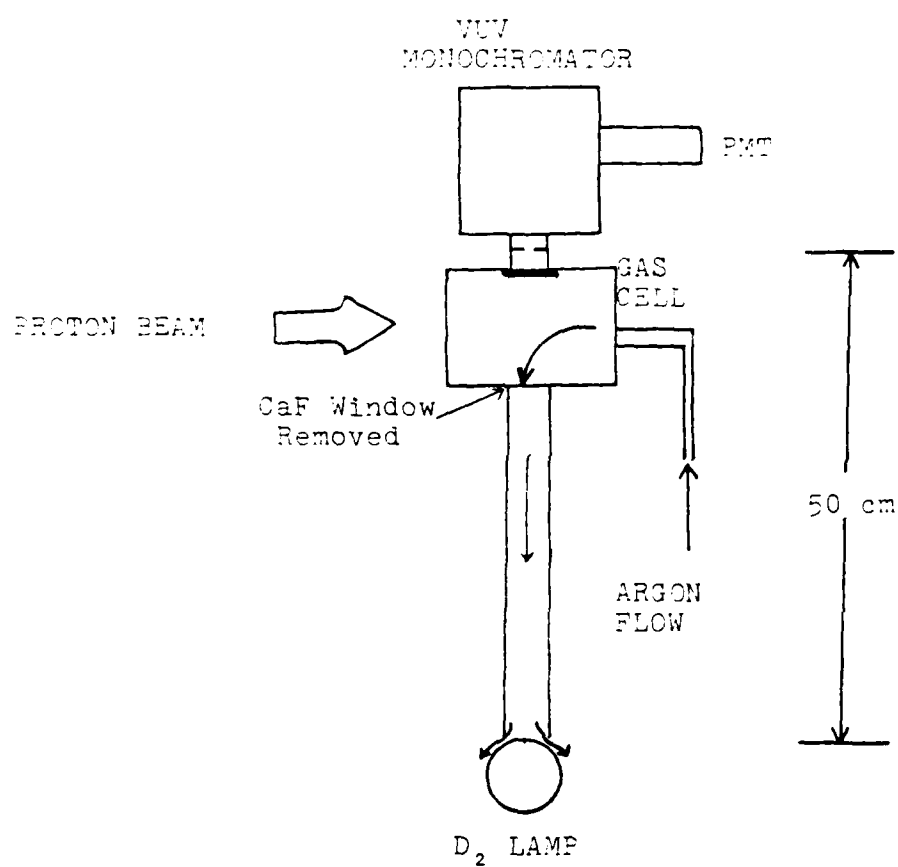


Figure 28. Setup for Monochromator Calibration.
Arrows denote argon gas flow.

Wavelength (nm)	Spectral Irradiance (W/cm ³)
195.0	.489
190.0	.475
185.0	.448
180.0	.378
175.0	.296
170.0	.230
168.0	.246
164.0	.460
163.6	.751
163.4	.992
163.1	1.23
162.8	1.15
162.5	.918
162.0	1.13
161.8	1.22
161.6	1.42
161.4	1.80
161.2	2.39
161.0	2.70
160.8	2.54
160.4	1.63
160.2	1.36
160.0	1.26
159.4	1.28
159.0	1.34

*Note: The measured irradiances for all wavelengths < 168 nm arise from the blending of molecular lines. Therefore these values are dependent upon the wavelength bandpass used for the measurement. The values given are for a triangular-shaped slit function with full width at half maximum of 0.42 nm.

Table 3.* Spectral Irradiance of Lamp at 50 cm for current of 300 ma.

Wavelength scans were taken at increasing argon flow rates until no change in the intensity at 160 nm was observed. Scans were then taken, and the efficiency was calculated.

The deviation below is essentially that of Monahan²⁷. When a source of known irradiance is used, the number of counts registered by the MCA in a given channel is given by the expression

$$S'(\bar{\lambda}_n) = \iint_{t-\frac{\beta}{2}}^{\lambda+\frac{\beta}{2}} K(\lambda') E(\lambda') A_s d\lambda' dt \quad 1)$$

where

$E(\lambda')$ = photon flux per nm at 50 cm from source

$K(\lambda')$ = efficiency of monochromator system

β = band pass of monochromator

A_s = slit area in cm^2

$S'(\bar{\lambda}_n)$ = number of counts in channel n of scan.

The time integration is performed over the time per channel, in all cases this is 1 sec. Performing the time integration, we have

$$S'(\bar{\lambda}_n) = A_s T \int_{\lambda-\frac{\beta}{2}}^{\lambda+\frac{\beta}{2}} K(\lambda') E(\lambda') d\lambda' . \quad 2)$$

If we assume that $E(\bar{\lambda}_n)$ is approximately constant over the wavelength interval scanned during the time T, we can write;

$$S'(\bar{\lambda}_n) = A_s TE(\bar{\lambda}_n) \int_{\lambda - \frac{\beta}{2}}^{\lambda + \frac{\beta}{2}} K(\lambda') d\lambda' \quad . \quad 3)$$

From the triangular bandpass of the monochromator, we see;

$$S'(\bar{\lambda}_n) = A_s TE(\bar{\lambda}_n) K(\bar{\lambda}_n) \beta \quad 4)$$

Solving for $K(\bar{\lambda}_n)$, we obtain

$$K(\bar{\lambda}_n) = \frac{S'(\bar{\lambda}_n)}{A_s TE(\bar{\lambda}_n) \beta} \quad . \quad 5)$$

For a beam induced scan, a similar result can be obtained. The result is

$$S(\bar{\lambda}_n) = TA_s f_{ij}(\bar{\lambda}_n) K(\bar{\lambda}_n) \beta / (4\pi R^2) \quad 6)$$

where f_{ij} = photon production rate per nm from gas cell

R = distance from center of gas cell to entrance slit.

Solving Eq. 6 for f_{ij}

$$f_{ij} = \frac{4\pi R^2 S(\bar{\lambda}_n)}{TA_s K(\bar{\lambda}_n) \beta} \quad 7)$$

The units for f_{ij} are photons \cdot sec $^{-1}$ \cdot nm $^{-1}$.

If we now sum f_{ij} over all wavelengths scanned, multiplied by the band width of the monochromator, we obtain

$$F_{ij} = \frac{4\pi R^2}{TA_s} \sum_{i=1}^N \frac{S(\bar{\lambda}_i)}{K(\bar{\lambda}_i)} . \quad 8)$$

We see now, we have the total photon production rate from the gas cell. Converting this to the energy emitted, we have

$$E_{ij} = \frac{4\pi R^2 hc}{TA_s} \sum_{i=1}^N \frac{S(\bar{\lambda}_i)}{K(\bar{\lambda}_i) \bar{\lambda}_i} . \quad 9)$$

This is equivalent to the last equation of Chapter III.

Computation of Efficiency

Using Eq. 5 of this Appendix, a computer program was written to calculate the efficiency at the wavelengths supplied by NBS. The efficiency as a function of wavelength is given in Figure 28. The solid line in Figure 28 is a least squares polynomial fit to the data through fourth order. The least squares coefficients are given in Table 4.

With this functional form of the efficiency, Eq. 9 was used to calculate the energy emitted from the gas cell. From the program given in Appendix A, the input

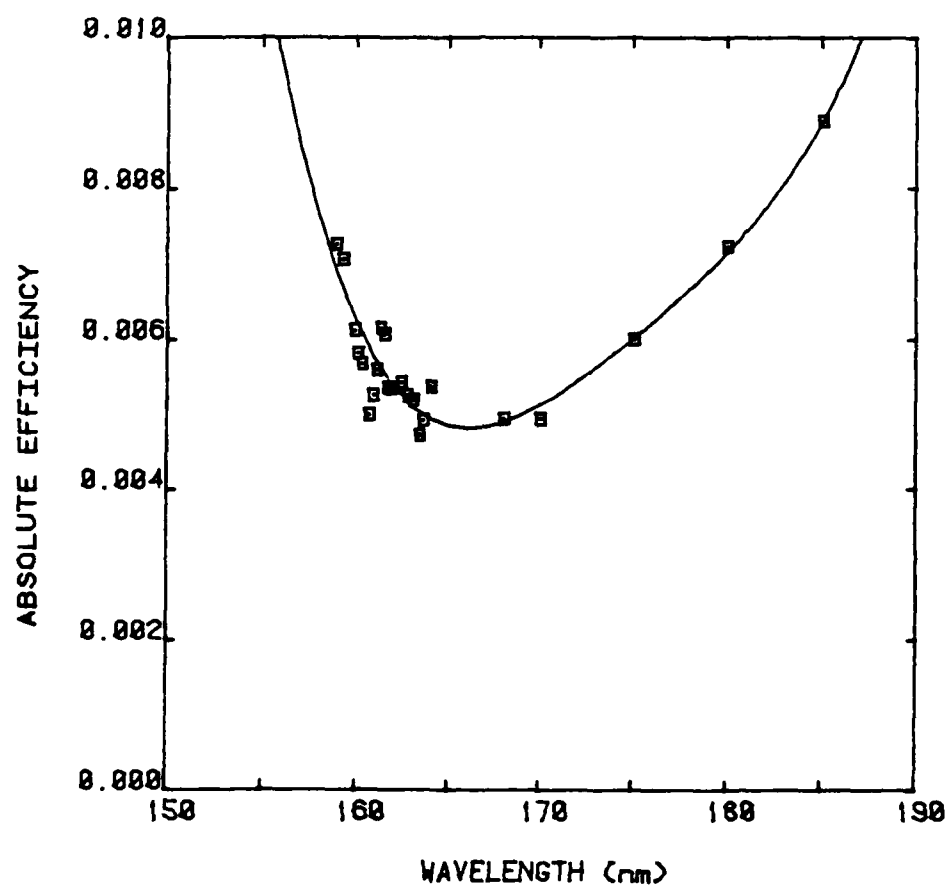


Figure 29. Absolute Efficiency of VUV Monochromator.

$$a_1 = 43.9378$$

$$a_2 = 1.00315$$

$$a_3 = 8.5901 \times 10^{-3}$$

$$a_4 = 3.2700 \times 10^{-5}$$

$$a_5 = 4.6701 \times 10^{-8}$$

Table 4. Least Squares Coefficients for the solid line in Figure 28. The equation is of the form

$$\text{Efficiency} = \sum_{i=1}^5 a_i \lambda^{i-1}$$

energy could be calculated. The ratio of the output energy to the input energy is the conversion efficiency, as discussed in Chapter III.

APPENDIX C

SOLUTION TO THE DIFFERENTIAL EQUATIONS
GOVERNING THE POPULATIONS OF THE
EXCIMER SYSTEM, Xe_2^*

The differential equations, for the resonance and metastable states, are given by:

$$\frac{dR}{dt} = -k_1 P^2 R - k_4 PR + k_3 PM - \frac{R}{\tau_1} \quad 1)$$

$$\frac{dM}{dt} = -k_2 P^2 M - k_3 PM + k_4 PR \quad . \quad 2)$$

$$\text{If we define } \lambda_1 = k_1 P^2 + k_4 P + \frac{1}{\tau_1} \quad 3)$$

$$\lambda_2 = k_2 P^2 + k_3 P \quad , \quad 4)$$

we have

$$\frac{dR}{dt} = -\lambda_1 R + k_3 PM \quad 5)$$

$$\frac{dM}{dt} = -\lambda_2 M + k_4 PR \quad . \quad 6)$$

Using the symbolic operator, $D = \frac{d}{dt}$, we obtain

$$(D+\lambda_1)R - k_3 PM = 0 \quad 7)$$

$$(D+\lambda_2)M - k_4 PR = 0 \quad . \quad 8)$$

We can solve Eqs. 7 and 8 simultaneously by multiplying Eq. 7 by $(D+\lambda_2)$ and Eq. 8 by $k_3 P$, yielding

$$(D+\lambda_2)(D+\lambda_1)R - (D+\lambda_2)k_3 PM = 0 \quad 9)$$

$$k_3 P(D+\lambda_2)M - k_4 k_3 P^2 R = 0 \quad . \quad 10)$$

Adding Eqs. 9 and 10 together, we obtain

$$(D+\lambda_2)(D+\lambda_1)R - k_1 k_3 P^2 R = 0 \quad 11)$$

$$[D^2 + (\lambda_1 + \lambda_2)D + \lambda_1 \lambda_2]R - k_4 k_3 P^2 R = 0 \quad . \quad 12)$$

This homogeneous, linear, differential equation has an auxillary equation which is

$$M^2 + (\lambda_1 + \lambda_2)M + (\lambda_1\lambda_2 - k_4k_3P^2) = 0 \quad 13)$$

so that

$$M = \frac{-(\lambda_1 + \lambda_2) \pm \sqrt{(\lambda_1 + \lambda_2)^2 - 4(\lambda_1\lambda_2 - k_4k_3P^2)}}{2}^{1/2} \quad 14)$$

$$M = \frac{-(\lambda_1 + \lambda_2) \pm \sqrt{(\lambda_1 - \lambda_2)^2 + 4k_4k_3P^2}}{2}^{1/2} \quad 15)$$

calling

$$M_1 = \frac{-(\lambda_1 + \lambda_2) + \sqrt{(\lambda_1 - \lambda_2)^2 + 4k_4k_3P^2}}{2}^{1/2} \quad 16)$$

$$M_2 = \frac{-(\lambda_1 + \lambda_2) - \sqrt{(\lambda_1 - \lambda_2)^2 + 4k_4k_3P^2}}{2}^{1/2} \quad 17)$$

we have

$$R(t) = C_1 e^{-M_1 t} + C_2 e^{-M_2 t} \quad 18)$$

where C_1 and C_2 are determined from the initial conditions

$$R(t) \Big|_{t=0} = R_0$$

From experimental data, $(\lambda_1 - \lambda_2)^2 \gg 4k_4k_3P^2$, so the expression for $R(t)$ reduces to

$$R(t) = R_0 e^{-\lambda_1 t} + R_0 e^{-\lambda_2 t} \quad 19)$$

So we see that the decay of the resonance line should have a two component decay. At all pressures, $\lambda_2 < \lambda_1$, so the fast component gives us information concerning

the $^3\Sigma$ formation while the slow component tells us about the $^1\Sigma$ formation. The small size of the slow component precluded any meaningful analysis.

Using Eq. 19, and substituting into Eq. 6, we can find the metastable population, which is not directly observable in this experiment. The result is

$$\frac{dM}{dt} + \lambda_2 M = k_4 P [R_0 (e^{-\lambda_1 t} + e^{-\lambda_2 t})] . \quad (20)$$

Eq. 20 can be solved by a variety of techniques; Laplace transforms will be used here. Taking the transform of Eq. 20, we have

$$sY - M_0 + \lambda_2 Y = k_4 PR_0 \left(\frac{1}{s+\lambda_1} + \frac{1}{s+\lambda_2} \right) \quad (21)$$

where Y = Laplace transform of M ,

M_0 = initial population of metastable atoms.

Solving for Y , we obtain

$$Y = \frac{k_4 PR_0}{(s+\lambda_2)} \left[\frac{1}{(s+\lambda_1)} + \frac{1}{(s+\lambda_2)} \right] + \frac{M_0}{s+\lambda_2} \quad (22)$$

$$Y = \frac{k_4 PR_0}{(s+\lambda_2)(s+\lambda_1)} + \frac{k_4 PR_0}{(s+\lambda_2)^2} + \frac{M_0}{(s+\lambda_2)} . \quad (23)$$

Taking inverse transforms

$$M = \frac{k_4 PR_0}{(\lambda_1 - \lambda_2)} [e^{-\lambda_2 t} - e^{-\lambda_1 t}] + k_4 PR_0 t e^{-\lambda_2 t} + M_0 e^{-\lambda_2 t} \quad (24)$$

$$M = \left[\frac{k_4 PR_0}{\lambda_1 - \lambda_2} + k_4 PR_0 t + M_0 \right] e^{-\lambda_2 t} - \frac{k_4 PR_0}{\lambda_2 - \lambda_1} e^{-\lambda_1 t} . \quad (25)$$

As we see, the metastable population will also have a two component exponential time dependence, very similar to that of the resonance state population.

We can now find the time dependence of the two molecular states. The differential equations which govern their time dependence are

$$\frac{dU}{dt} = k_1 P^2 R - \frac{U}{\tau_3} \quad 26)$$

$$\frac{dL}{dt} = k_2 P^2 M - \frac{L}{\tau_2} . \quad 27)$$

These are the same as Eqs. 10 and 11 of Chapter IV. From Eq. 26 and 19, we have

$$\frac{dU}{dt} = k_1 P^2 [R_0(e^{-\lambda_1 t} + e^{-\lambda_2 t})] - \frac{U}{\tau_3} \quad 28)$$

$$\frac{dU}{dt} + \frac{U}{\tau_3} = k_1 P^2 R_0 (e^{-\lambda_1 t} + e^{-\lambda_2 t}) . \quad 29)$$

Using Laplace Transforms, we see

$$sZ + \lambda_3^{-1}Z = k_1 P^2 R_0 \left(\frac{1}{s+\lambda_1} + \frac{1}{s+\lambda_2} \right) \quad 30)$$

where the initial condition is

$$U \Big|_{t=0} = 0 .$$

Solving for Z , we obtain

$$Z = \frac{k_1 P^2 R_0}{(s+\tau_3^{-1})} \left(\frac{1}{s+\lambda_1} + \frac{1}{s+\lambda_2} \right) . \quad 31)$$

AD-A104 094 AUBURN UNIV ALA DEPT OF PHYSICS F/G 7/4
INTENSE PULSED PROTON SOURCE (TIME AND WAVELENGTH RESOLVED STUD--ETC(U))
JUN 81 J R WILLIAMS, J E GAISER DASG60-79-C-0079
UNCLASSIFIED NL

2 OF 2

50-0032



END
DATE FILMED
10 81
DTIC

Inverting the transform, we get

$$U(t) = \frac{k_1 P^2 R_0}{(\lambda_1 - \frac{1}{\tau_3})} [e^{-\lambda_1 t} - e^{-\frac{t}{\tau_3}}] + \frac{k_1 P R_0}{(\lambda_2 - \frac{1}{\tau_3})} [e^{-\lambda_2 t} - e^{-\frac{t}{\tau_3}}] \quad (32)$$

Grouping like exponentials, we have

$$U(t) = \frac{k_1 P^2 R_0}{(\lambda_1 - \frac{1}{\tau_3})} e^{-\lambda_1 t} + \frac{k_1 P^2 R_0}{(\lambda_2 - \frac{1}{\tau_3})} e^{-\lambda_2 t} + [\frac{k_1 P^2 R_0}{(\lambda_1 - \frac{1}{\tau_3})} - \frac{k_1 P^2 R_0}{(\lambda_2 - \frac{1}{\tau_3})}] e^{-\frac{t}{\tau_3}} \quad (33)$$

This shows that the decay of the ${}^1\Sigma_u^*$ state in Xe_2^* should have a three component exponential. The observed data shows only a two exponential dependence, indicating that the contribution of the second term in Eq. 33 is rather small and masked by the presence of terms one and three, as seen in the pressure dependence of the data.

Finally, we solve for the ${}^3\Sigma_u^*$ population as a function of time. Eqs. 27 and 25 give

$$\frac{dL}{dt} = k_2 P^2 [D e^{-\lambda_2 t} - D' e^{-\lambda_1 t}] - \frac{L}{\tau_2} \quad (34)$$

where $D = \frac{k_4 P R_0}{\lambda_1 - \lambda_2} + k_4 R_0 P t + M_0$

$$D' = \frac{k_4 P R_0}{\lambda_2 - \lambda_1}$$

Again using Laplace Transforms, with the initial condition of zero population, we have

$$\frac{dx}{dt} + \frac{x}{\tau_2} = k_2 P^2 [D e^{-\lambda_2 t} - D' e^{-\lambda_1 t}] \quad 35)$$

$$x = \frac{k_2 P^2}{s + \frac{1}{\tau_2}} \left[\frac{D}{s + \lambda_2} - \frac{D'}{s + \lambda_1} \right] \quad . \quad 36)$$

Inverting the transform yields

$$L(t) = \frac{k_2 P^2 D}{\lambda_2 - \frac{1}{\tau_2}} [e^{-\frac{t}{\tau_2}} - e^{-\lambda_2 t}] - \frac{k_2 P^2 D'}{\lambda_1 - \frac{1}{\tau_2}} [e^{-\frac{t}{\tau_2}} - e^{-\lambda_1 t}] \quad . \quad 37)$$

Grouping like exponentials gives us

$$L(t) = \frac{k_2 P^2 D}{\lambda_2 - \frac{1}{\tau_2}} e^{-\lambda_2 t} + \frac{k_2 P^2 D'}{\lambda_1 - \frac{1}{\tau_2}} e^{-\lambda_1 t} + \left[\frac{k_2 P^2 D}{\lambda_2 - \frac{1}{\tau_2}} - \frac{k_2 P^2 D'}{\lambda_1 - \frac{1}{\tau_2}} \right] e^{-\frac{t}{\tau_2}} \quad . \quad 38)$$

We see this is very similar to the ${}^1\Sigma_u$ state decay, as expected from the simplicity and symmetry of the system.

APPENDIX D
ABBREVIATIONS AND CONVERSION FACTORS

ABBREVIATIONS AND CONVERSION FACTORS

<u>Abbreviation</u>	<u>Meaning</u>
cm	centimeter
nm	nanometer
VUV	vacuum ultraviolet
eV	electron volt
MeV	million electron volt
μs	microsecond
ns	nanosecond
kA	kilo ampere
MV	million volt
BPO	beam pick off
PPM	parts per million
sccm	standard cubic centimeter per minute
SPC	single photon counting
CFD	constant fraction discriminator
TAC	time to amplitude converter
SCA	single channel analyzer
MCA	multichannel analyzer
PMT	photomultiplier tube
UHV	ultra high vacuum
UV-V	ultraviolet-visible
Hz	Hertz = sec ⁻¹
MHz	megahertz

Conversion Factor

$$1 \text{ Hz/Torr} = 3.12 \times 10^{16} \text{ cm}^3/\text{sec}$$

$$1 \text{ Hz/Torr}^2 = 9.75 \times 10^{32} \text{ cm}^6/\text{sec}^2$$

APPENDIX E
DATA FOR FIGURES 18 and 19

DATA FOR FIGURE 18

<u>Pxe (Torr)</u>	<u>DF (MHz)</u>
50	.414
103	1.00
207	3.31
303	6.73
405	11.83
505	17.89
604	24.55

DATA FOR FIGURE 19

<u>Pxe (Torr)</u>	<u>DF (MHz)</u>
45	.347
56	.350
79	.532
97	.730
122	1.06
154	1.39
184	1.85

END
DATE
FILMED
10-81
DTIC